Molecular mapping and functional validation of GLP-1R cholesterol binding sites in pancreatic beta cells

Affiong I Oqua[1], Kin Chao[2], Liliane El Eid[1], Lisa Casteller[2], Alba Miguéns[3], Sebastian Barg[3], Ben Jones[4], Jorge Bernadino de la Serna[5,*], Sarah L Rouse[2,*] and Alejandra Tomas[1,*]

[1] Section of Cell Biology and Functional Genomics, Division of Diabetes, Endocrinology and Metabolism, Department of Metabolism, Digestion and Reproduction, Imperial College London, London, UK.

[2] Department of Life Sciences, Imperial College London, London, UK.

[3] Department of Medical Cell Biology, University of Uppsala, Uppsala, Sweden.

[4] Section of Investigative Medicine, Division of Diabetes, Endocrinology and Metabolism, Department of Metabolism, Digestion and Reproduction, Imperial College London, London, UK.

[5] National Heart and Lung Institute, Imperial College London, London, UK.

*Corresponding authors:

a.tomas-catala@imperial.ac.uk (A.T.)

s.rouse@imperial.ac.uk (S.L.R.)

j.bernardino-de-la-serna@imperial.ac.uk (J.B.S.)

Abstract

G protein-coupled receptors (GPCRs) are integral membrane proteins which closely interact with their plasma membrane lipid microenvironment. Cholesterol is a plasma membrane enriched lipid with pivotal roles in the control of membrane fluidity and maintenance of membrane microarchitecture, directly impacting on GPCR stability, dynamics and function. Cholesterol extraction from pancreatic beta cells has previously been shown to disrupt the internalisation, clustering and cAMP responses of the glucagon-like peptide-1 receptor (GLP-1R), a class B1 GPCR with key roles in the control of blood glucose levels via the potentiation of insulin secretion in beta cells and weight reduction via the modulation of brain appetite control centres. Here, we unveil the detrimental effect of a high cholesterol diet on GLP-1R-dependent glucoregulation *in vivo*, and the improvement in GLP-1R function that a reduction in cholesterol synthesis using simvastatin exerts in pancreatic islets. We next identify and map sites of cholesterol high occupancy and residence time on active *versus* inactive GLP-1Rs using coarse-grained molecular dynamics (cgMD) simulations, followed by a screen of key residues selected from these sites and detailed analyses of the effects of mutating one of these residues, Val229, to alanine on GLP-1R interactions with cholesterol, plasma membrane behaviours, clustering, trafficking and signalling in pancreatic beta cells and primary islets, unveiling an improved insulin secretion profile for the V229A mutant receptor. This study 1) highlights the role of cholesterol in regulating GLP-1R responses *in vivo*; 2) provides a detailed map of GLP-1R - cholesterol binding sites in model membranes; 3) validates their functional relevance in beta cells; and 4) highlights their potential as locations for the rational design of novel allosteric modulators with the capacity to fine-tune GLP-1R responses.

Introduction

The glucagon-like peptide-1 receptor (GLP-1R), expressed in pancreatic beta cells amongst other tissues including brain, lung, stomach, and heart, is activated by the incretin peptide hormone GLP-1, secreted from enteroendocrine L-cells after food intake (1), to regulate postprandial glucose levels via the potentiation of glucose-dependent insulin secretion (2-4). Activation of GLP-1R also promotes beta cell survival, inhibits gastric emptying, regulates food intake and reduces appetite (1, 5), making it a key pharmacological target for various metabolic disorders including type 2 diabetes (T2D) and obesity (6, 7). Circulation of active GLP-1(7-36) hormone is short-lived due to its rapid cleavage into inactive GLP-1(9-36) by dipeptidyl peptidase-4 (DPP-4) (2); peptide analogues of GLP-1 have therefore been developed and successfully used clinically for the treatment of T2D and obesity, including exendin-4, liraglutide, and semaglutide, amongst others (1, 2, 5). Despite their success, access to incretin peptide analogues is challenging for most individuals that require these therapies due to their high cost and complex manufacturing process leading to supply shortages, as well as requirement for refrigeration and administration by injection, together with notable side effects including gastrointestinal disturbances, prompting further research into the development of a new wave of small molecules (8, 9), including those targeting the receptor as allosteric or ago-allosteric modulators (10, 11).

The GLP-1R is part of the glucagon family of receptors, including the glucose-dependent insulinotropic polypeptide receptor (GIPR) (5), the glucagon receptor (GCGR) (12), and the glucagon-like peptide-2 receptor (GLP-2R) (13), which are class B1/secretin-like G protein-coupled receptors (GPCRs) with a typical structure of seven transmembrane domains (7-TMD), a C-terminal tail, and a large N-terminal extracellular domain (ECD) important for peptide agonist binding (14). GPCRs transmit extracellular signals via coupling to heterotrimeric G proteins and interactions with β-arrestins, leading to activation of various intracellular signalling cascades (15); the GLP-1R in particular signals preferentially via $G\alpha_s$ coupling and adenylate cyclase activation, leading to cAMP accumulation and downstream signal transduction (16). Their 7-TMD structure involves intimate interactions with plasma membrane lipids (15), known to be non-homogeneously distributed but rather organised in regions known as lipid nanodomains or lipid rafts, enriched in lipid species including sphingolipids and cholesterol, as well as in integral membrane proteins serving as scaffolds for signal transduction (17, 18), and GPCR trafficking and sorting (15, 19, 20).

Cholesterol, in particular, has been identified as an allosteric modulator for certain GPCRs, due to its direct binding to (21, 22) and modulation of GPCR activation, trafficking, and signalling patterns (23, 24). A previous study from our laboratory established that the GLP-1R function in pancreatic beta cells is also modulated by cholesterol. Specifically, we showed that GLP-1R activation leads to receptor segregation into flotillin-positive lipid nanodomains and that disruption of the plasma membrane architecture by cholesterol extraction with methyl-β-cyclodextrin (MβCD) significantly reduces exendin-4-mediated receptor clustering, internalisation, and cAMP accumulation in beta cells (25). Here, we focus on identifying the effect of more nuanced changes in cholesterol content on exendin-4-mediated GLP-1R function in primary islets and *in vivo*, followed by mapping of cholesterol binding sites for both apo-state and active receptor structures using coarse-grained molecular dynamics (cgMD) simulations tailored to identify lipid-receptor interactions, and functional validation of a prominent site for its effects on cholesterol binding, plasma membrane behaviours and exendin-4-mediated GLP-1R function in beta cells and primary islets. Our investigation

identifies new potentially druggable locations in the receptor, expanding the existing repertoire of functionally relevant sites for the rational design of novel GLP-1R allosteric modulators based on the modulation of receptor-cholesterol interactions.

Results

Changes in cholesterol content modulate exendin-4-induced GLP-1R behaviours in primary islets and in vivo

To determine the effect of increased cholesterol levels on GLP-1R function, we fed mice a standard chow diet supplemented or not with cholesterol for 5 weeks. We then performed intraperitoneal glucose tolerance tests (IPGTTs) post-administration of vehicle or 1 nmol/kg exendin-4 to determine the glucose lowering effect of pharmacologically targeting the receptor under these conditions. Mice on either diet had similar glucose responses under vehicle conditions; however, those on high cholesterol diet presented worse glucose lowering responses to exendin-4 *versus* chow-fed mice (Figure 1A, B), an effect that was maintained when normalised to the corresponding vehicle control (Figure 1C). Moreover, islets extracted from high cholesterol-fed mice showed decreased exendin-4-induced cAMP responses *ex vivo* (Supplementary Figure 1A), suggesting a direct impact of increased cholesterol levels on GLP-1R signalling.

To further evaluate the effect of increased islet cholesterol content on GLP-1R function, islets isolated from wildtype (WT) mice were loaded with MβCD saturated with cholesterol, which led to a significant increase in cholesterol content (Figure 1D). Under these conditions, we measured a decrease in insulin secretion in response to exendin-4 *versus* vehicle conditions, primarily due to elevated basal secretion levels at 11 mM glucose (Figure 1E, F), confirming that increased cholesterol levels reduce the GLP-1R glucoregulatory potential by decreasing its capacity to potentiate islet insulin secretion.

We next performed the reverse experiment by decreasing islet cholesterol levels with simvastatin, a long-established hydroxy-methylglutaryl coenzyme A reductase (HMGCR) inhibitor (26). Filipin staining confirmed decreased islet cholesterol content (Figure 1G), which correlated with increased exendin-4-induced cAMP responses (Supplementary Figure 1B), and exendin-4-induced insulin secretion (Figure 1H, I) in simvastatin-exposed islets. These effects were accompanied by decreased GLP-1R plasma membrane diffusion under vehicle conditions, measured by Raster Image Correlation Spectroscopy (RICS) in rat insulinoma INS-1 832/3 cells with endogenous GLP-1R deleted [INS-1 832/3 GLP-1R KO cells (27)] stably expressing SNAP/FLAG-tagged human GLP-1R (SNAP/FLAG-hGLP-1R), an effect that is normally triggered by agonist binding (28), as also observed here (Supplementary Figure 1C, D). Taken together, these results demonstrate that changes in cholesterol levels have specific effects on beta cell GLP-1R behaviours, indicating the potential existence of direct interactions between the receptor and this plasma membrane-enriched lipid.

Coarse-grained molecular dynamics simulations reveal GLP-1R cholesterol binding sites and state-dependent cholesterol binding modes

To gain insights into the precise location of cholesterol interactions with the GLP-1R, cgMD simulations were employed to study both active (corresponding to agonist bound) and inactive (apo-) states of GLP-1R in a model mammalian plasma membrane using the latest Martini 3

forcefield and cholesterol parameters (Figure 2A). The PyLipID package (29) was employed to characterise cholesterol interactions for each receptor state. Two key parameters were measured: occupancy, defined as the percentage of frames in the trajectory where any cholesterol molecule is within the cutoff distance from the receptor, and interaction residence time, defined as the time that a cholesterol molecule remains in the binding site, providing information about the strength of the interaction (full data included in Supplementary Tables 1 and 2). Occupancy values for each receptor residue in both states were calculated and displayed as heatmaps, with the top 10 residues per state indicated in Figure 2B. The receptor active and inactive states exhibited similar top occupancy residues, with hydrophobic residues such as Phe, Leu, Ile, and Val enriched in both states. A generally similar profile was observed for the top 30 highest occupancy residues in active *versus* inactive states, with some subtle differences noted in the receptor transmembrane domains TM2 and TM6 (Figure 2C).

The top three cholesterol binding sites, displaying the highest cholesterol residence times for both states, were calculated using the PyLipID package (Figure 2D, E). Interestingly, notable differences were observed in these sites between the two receptor states: for the active state, site I (purple) was located in the upper TM1 and TM7 region, while in the inactive state, site I (cyan) was found in the lower TM5 and TM6 region, an area which undergoes key structural changes upon G protein engagement and GLP-1R activation (30) and might therefore represent a state-specific cholesterol binding site. Site II (orange) was similar for both states but presented subtle differences, with an additional cholesterol pocket involving the Trp in extracellular loop 2 (ECL2) being more pronounced in the inactive *versus* the active state. Site III (green) showed some degree of variation between the two states; in the inactive state, two TM5 residues (Val319 and Phe315) formed an additional cholesterol pocket with TM4, presenting the highest average residence time (186 ns) across all sites, while, in the active state, the cholesterol pocket was located closer to the bottom of TM3 and TM4, involving Leu260 in ECL2.

To evaluate the functional relevance of the GLP-1R cholesterol binding sites identified during the cgMD simulations, 12 residues were selected within or at the periphery of these sites and mutated to alanine by site-directed mutagenesis (Figure 2F). Alanine mutations for four of the selected residues (Ile323, Val160, Gly151, and His363) were predicted to cause changes in the GLP-1R structure in the active state by altering the cavity or causing changes in exposed residues and breakages in salt bridges between residues, while a further three alanine mutated residues (Val229, Gly151, and His363) were predicted to cause changes in the inactive GLP-1R structure (Figure 2G). SNAP/FLAG-tagged human GLP-1Rs (SNAP/FLAG-hGLP-1Rs) with single alanine substitutions for each selected residue were successfully expressed in INS-1 832/3 GLP-1R KO cells with no significant differences detected in cell surface expression levels *versus* WT GLP-1R (Figure 2H, top graph). Mutant receptors were then screened for their capacity to undergo exendin-4-induced internalisation, as this GLP-1R property is severely inhibited following cholesterol extraction with MβCD (31). Four alanine mutated residues, V229A, V160A, I165A, and L401A, caused a significant decrease in GLP-1R internalisation *versus* WT receptor, with GLP-1R V229A and V160A causing a ~40%, and I165A and L401A a ~30% decrease in internalisation (Figure 2H, bottom graph). GLP-1R V229A was selected for further detailed analysis of the effects of modifying a GLP-1R-cholesterol binding site residue on GLP-1R beta cell behaviours.

GLP-1R V229A substitution affects GLP-1R-cholesterol interactions and plasma membrane behaviours in pancreatic beta cells

We next generated INS-1 832/3 GLP-1R KO sublines stably expressing SNAP/FLAG-hGLP-1R WT or V229A. As expected, no difference in surface expression was detected between WT and V229A receptors (Figure 3A, B). To determine the effect of the V229A substitution on the overall GLP-1R binding to cholesterol in active *versus* inactive conditions, cells from both sublines were labelled with PhotoClick cholesterol and exposed to UV light prior to SNAP/FLAG-hGLP-1R purification by anti-FLAG immunoprecipitation and click chemistry to fluorescently label covalently bound PhotoClick cholesterol (Figure 3C). Resulting samples were separated by SDS-PAGE and gels imaged under fluorescence followed by anti-SNAP Western blotting (Supplementary Figure 2A). Quantification of GLP-1R-bound cholesterol in both WT and V229A receptors following vehicle *versus* acute (2 minute) exendin-4 stimulation showed a significant decrease in cholesterol binding to GLP-1R V229A in vehicle conditions without modifying cholesterol binding after agonist stimulation compared to GLP-1R WT (Figure 3D). Co-localisation of SNAP/FLAG-hGLP-1R with cholesterol in the same cells using the fluorescent D4H*-mCherry probe to label plasma membrane cholesterol at the cytosolic leaflet (32) corroborated our previous results as we measured a significant decrease in co-localisation between GLP-1R V229A and cholesterol under vehicle conditions compared to WT GLP-1R (Figure 3E-G).

While we could not measure any changes in receptor conformational shift following exendin-4 binding between GLP-1R WT and V229A (Supplementary Figure 2B, C), quantification of GLP-1R plasma membrane diffusion coefficients using RICS in INS-1 832/3 SNAP/FLAG-hGLP-1R WT *versus* V229A cells revealed a pronounced reduction in GLP-1R V229A plasma membrane diffusion compared to WT GLP-1R under vehicle conditions (Figure 4A, B), to a similar extent to the reduction caused by exendin-4 binding to GLP-1R WT, as observed here and previously (33), and recapitulating the effect triggered by reduced cholesterol levels following simvastatin exposure (Supplementary Figure 1C, D). Single particle tracking (SPT) of human GLP-1R fused to monoclonal EGFP (hGLP-1R-mEGFP) WT *versus* V229A imaged by total internal reflection fluorescence (TIRF) microscopy also showed reduced total displacement and speed (displacement over time) of V229A *versus* WT receptors under vehicle conditions, with these parameters also decreased following WT GLP-1R stimulation with exendin-4 (Figure 4C). Finally, exendin-4-induced activation of both WT and V229A GLP-1R tended to reduce the diffusion of lipids at the plasma membrane labelled with the environmentally sensitive Laurdan probe (34) (Figure 4D), with no differences in Laurdan lateral diffusion between WT and V229A. RICCS cross-correlation analysis of Laurdan-labelled lipid co-diffusion with GLP-1R WT *versus* V229A demonstrated a reduction in the movement of the GLP-1R-lipid complex for WT receptors after exendin-4 stimulation, with a tendency for V229A receptors to exhibit the same effect under vehicle conditions, resulting in no significant change for GLP-1R V229A-lipid complex diffusion between vehicle and exendin-4-stimulated conditions (Figure 4E, Supplementary Figure 2D).

Number and Brightness (N&B) analysis of the RICCS cross-correlation data was then used to determine the effect of the V229A substitution on receptor oligomerisation before and after exendin-4 stimulation (Figure 5A). Both WT and V229A receptors existed predominantly as monomers or dimers at a proportion of ~60 to 80% of total receptors, a percentage that was reduced for the WT receptor at later acquisition times under vehicle conditions, but with otherwise few changes following exendin-4 stimulation. Around 30% of inactive WT or V229A receptors existed as dimers to hexamers or hexamers to decamers, with a tendency for the dimer to hexamer population to reduce and the hexamer to decamer population to increase after exendin-4 stimulation, and for GLP-1R V229A to have a higher proportion of hexamers

to decamers under vehicle conditions *versus* WT receptors. A smaller proportion of receptors existed as higher order oligomers, with a significant increase measured for the WT GLP-1R after stimulation with exendin-4. For the GLP-1R V229A, however, we observed a higher proportion of receptors pre-existing as higher order oligomers under vehicle conditions, with no further increases after exendin-4 stimulation, indicating that the mutant receptor has a higher clustering propensity in the inactive state. Consistent with this finding, GLP-1R V229A also presented with significantly increased levels of receptors segregated to lipid rafts (35) prior to exendin-4 stimulation *versus* GLP-1R WT (Figure 5B).

To determine if the V229A substitution affected receptor recruitment to clathrin-coated pits (CCPs) after agonist stimulation, TIRF images were acquired of both unstimulated and exendin-4-stimulated INS-1 832/3 SNAP/FLAG-hGLP-1R WT *versus* V229A cells (Figure 5C). Before agonist addition, the SNAP/FLAG-hGLP-1R signal was distributed across the plasma membrane and only weakly associated with clathrin-positive regions ($\Delta F/S = 0.03 \pm 0.003$ and 0.04 ± 0.006 for WT and V229A, respectively), with no differences between WT and V229A receptors. However, after exendin-4 stimulation, the receptor association with clathrin-positive regions increased, an effect that correlates with the known rapid GLP-1R internalisation triggered by exendin-4 (31), with this increase however significantly less pronounced for the GLP-1R V229A compared to WT ($\Delta F/S = 0.16 \pm 0.006$ and 0.10 ± 0.004 for WT *versus* V229A, respectively), in agreement with the reduced internalisation propensity displayed by this mutant receptor (Figure 2H).

GLP-1R V229A substitution affects receptor trafficking, activation and signalling in pancreatic beta cells

To determine the effects of the GLP-1R V229A substitution on GLP-1R trafficking, we assessed GLP-1R internalisation, recycling and degradation parameters in INS-1 832/3 SNAP/FLAG-hGLP-1R WT *versus* V229A cells. GLP-1R V229A internalised more slowly than WT receptor after exendin-4 stimulation (Figure 6A-C), with only ~10% of V229A internalised after 5-minutes stimulation *versus* ~30% for WT. V229A internalisation eventually recovered after 30 minutes of exendin-4 exposure, reaching ~50% for both receptor types. In contrast, plasma membrane recycling of internalised GLP-1R V229A was increased *versus* WT at both 1-hour and 3-hours recycling periods (Figure 6D, E), while no changes in exendin-4-induced GLP-1R degradation were detected between GLP-1R WT and V229A (Figure 6F, G).

Next, we performed NanoBiT complementation assays to determine the effect of the GLP-1R V229A substitution on receptor coupling to G proteins and β-arrestins, assessing mini-G_s, mini-G_q, and β-arrestin 2 recruitment dose response curves to WT *versus* V229A receptors after stimulation with a range of exendin-4 doses. Results showed a significant increase in both the potency and efficacy of mini-G_s recruitment to V229A *versus* WT GLP-1R (Figure 7A). Conversely, mini-G_q recruitment was not changed between WT and V229A GLP-1R (Figure 7B). Additionally, GLP-1R V229A caused a small but consistent increase in β-arrestin 2 recruitment compared to GLP-1R WT (Figure 7C). Bias calculations between mini-G_s and β-arrestin 2 recruitment showed that GLP-1R V229A is $G\alpha_s$-biased *versus* WT GLP-1R (Figure 7D). GLP-1R V229A also displayed increased activity at the plasma membrane (Figure 7E), with a tendency for increased activity also from endosomes without reaching statistical significance (Figure 7F).

To determine differences between GLP-1R WT and V229A beta cell downstream signalling, cAMP and insulin secretion responses to exendin-4 were investigated in INS-1 832/3 SNAP/FLAG-hGLP-1R WT and V229A. GLP-1R V229A displayed a tendency for increased exendin-4-induced cAMP AUC, with kinetic responses that appeared delayed but reached significantly higher maximal cAMP peak levels (Figure 8A, B). Compared to WT receptor, GLP-1R V229A caused a significant decrease in basal insulin secretion under vehicle (11 mM glucose alone) conditions (Figure 8C), which resulted in significantly increased insulin secretion fold-responses to exendin-4 (Figure 8D). We then determined the effect of GLP-1R V229A in primary mouse islets. To this end, SNAP/FLAG-hGLP-1R WT or V229A-expressing adenoviruses were transduced into islets extracted from mice lacking endogenous GLP-1R expression (GLP-1R KO, generated *in house*). Similarly to the stable INS-1 832/3 sublines, there was no difference in surface expression of GLP-1R WT *versus* V229A in these islets (Figure 8E, top row and F). GLP-1R V229A also caused a significant decrease in receptor internalisation *versus* WT GLP-1R following exendin-4 stimulation (Figure 8E, bottom row and G). Expression of GLP-1R V229A was again associated with significantly improved insulin secretion fold-increases to exendin-4, but in this case no changes were detected under 11 mM glucose alone conditions, with the improved fold being a consequence of enhanced insulin secretion *versus* WT GLP-1R during the exendin-4 stimulation period (Figure 8H, I).

Discussion

In this study, we have focused on assessing the potential for modulation of cholesterol interactions as a strategy to control GLP-1R responses in pancreatic beta cells. We have first shown that exogenous cholesterol increases via prolonged dietary changes lead to a decrease in the capacity of the GLP-1R for *in vivo* glucoregulation, without affecting glucose levels under vehicle conditions. Further investigations showed that GLP-1R-mediated cAMP responses were reduced in islets extracted from these mice, suggesting that a high cholesterol diet specifically impacts on beta cell GLP-1R activity. Similarly, acute cholesterol increases in mouse islets exposed to cholesterol-loaded MβCD decreased the GLP-1R capacity to potentiate insulin secretion, validating our observed *in vivo* effects. In agreement with previous reports (36), acute (1 hour) beta cell exposure to high cholesterol leads to increased insulin secretion under 11 mM glucose conditions, but the GLP-1R is unable to further potentiate secretion to the same extent than with unmodified cholesterol levels.

While we have observed a direct detrimental effect of a cholesterol-enriched diet on islet GLP-1R cAMP outputs, we cannot rule out that the reduced receptor capacity to lower blood glucose levels following cholesterol loading might encompass further negative effects of high cholesterol on GLP-1R downstream signalling. Persistently elevated mouse islet cholesterol levels have been shown to cause a decrease in the expression of cholesterol synthesis genes (*Hmgcr*) and increased expression of steroidogenic acute and regulatory protein (StAR), while also decreasing glucose-stimulated insulin secretion (37). StAR is a steroid biogenesis factor involved in cholesterol transport from the outer to the inner mitochondrial membrane (38) expressed at low levels in beta cells (39), with increased StAR expression linked to reduced beta cell mitochondrial function (40). We (41), and others (42), have shown that the GLP-1R plays an important role in the control of beta cell mitochondrial function, a key process for optimal insulin secretion (43), with our recent interactome results unveiling direct interactions between GLP-1R and cholesterol biosynthesis and metabolism factors located at ER-mitochondria membrane contact sites (41). It is therefore possible that high cholesterol might impact on the capacity of the GLP-1R to regulate mitochondrial and beta cell function via

altered expression and interaction with cholesterol regulatory enzymes, hindering the insulin secretion potentiation effect of the receptor.

Conversely, in this study we also found that a reduction in mouse islet cholesterol levels with simvastatin, which disrupts ER cholesterol synthesis by inhibiting HMGCR enzymatic activity (44-46), increased exendin-4-mediated cAMP and insulin secretion responses. While this partial reduction in cholesterol levels appears beneficial for beta cell GLP-1R function, we previously observed that a much more drastic cholesterol extraction using MβCD leads to the opposite effect, inhibiting agonist-induced GLP-1R cAMP responses (25), a result that we hypothesise is linked to the profound disruption of plasma membrane architecture caused by MβCD (47). The use of statins at higher concentrations than in the present study has been previously associated with varying effects on insulin secretion: simvastatin was shown to reduce, while pravastatin increased insulin secretion in response to glucose, with GLP-1 or exendin-4 exposure restoring secretory responses from statin-treated cells (48). Statin use has been associated with increased risk of T2D by poorly understood mechanisms involving both reduced insulin sensitivity and impaired beta cell insulin secretion (49), the latter ameliorated by GLP-1R agonist exposure (50). Considering our results as well as previous literature, we speculate that patients with increased cholesterol levels might also exhibit reduced beta cell responses to incretin therapies unless dyslipidaemia is subsequently ameliorated following weight loss. In addition, patients taking cholesterol modifying drugs like statins are particularly good candidates for incretin use as they might present with improved incretin responses that would also help prevent a potentially increased risk of developing T2D in this patient subset.

The GLP-1R, as an integral membrane protein and 7-TMD GPCR, tightly interacts with its lipid-rich plasma membrane microenvironment (51) and is also known to segregate to cholesterol-rich flotillin-positive lipid nanodomains upon activation (25). It is therefore plausible that direct interaction of cholesterol molecules with specific binding pockets in the GLP-1R might at least be partially responsible for cholesterol modulation of GLP-1R function. To test this possibility, we performed cgMD simulations of GLP-1R in active *versus* inactive conformations in a model mammalian plasma membrane using the latest Martini 3 forcefield and cholesterol parameters, identifying specific receptor sites with high cholesterol occupancies and residence times. The fact that the highest cholesterol occupancy residues identified correspond to either ring-containing (Phe) or branched (Val, Leu, Ile) amino acids suggests that these residue types might play important roles in cholesterol stabilisation at GLP-1R binding pockets. Importantly, the GLP-1R-cholesterol binding sites identified here do not overlap with previously predicted cholesterol consensus motifs (CCM) (22) or Cholesterol Recognition Amino Acid Consensus (CRAC) motifs (52) identified for other GPCRs, confirming the theory that GPCRs lack predictable primary sequence consensus motifs for cholesterol binding (53, 54). The GLP-1R-cholesterol binding sites also presented notable differences between active and inactive receptor conformations, suggesting that cholesterol binding is regulated by agonist binding and receptor activation. GLP-1R in its inactive apo-state is constantly moving but prefers to adopt a closed ECD conformation in absence of peptide binding (55). Active, peptide-bound receptors, on the other hand, adopt a more open conformation resulting from the peptide agonist interacting with the ECD, leading to prominent changes at TMD regions which stabilise G protein binding and activation (30, 53, 56). The conformational shift between the receptor in active and inactive states is therefore predicted to affect GLP-1R-cholesterol interactions, thereby leading to distinct active *versus* inactive cholesterol binding sites. Interestingly, one of the most prominent GLP-1R-cholesterol binding

sites identified here lies within the functionally important TM5-TM6 region required for G protein signal transduction, indicating the potential impact of cholesterol binding on GLP-1R activation and downstream signalling.

To investigate the importance of direct cholesterol interactions in modulating beta cell GLP-1R function, we have screened 12 residues selected from the cholesterol binding sites identified in our cgMD simulations, covering a wide range of occupancy, residence time, ability to tolerate the planned mutation, and varied locations within binding sites in active *versus* inactive states. Interestingly, the residues that had significant effects on GLP-1R internalisation while mutated to alanine were all non-polar branched amino acids, with some of these also predicted to cause changes in the cavity in which they reside. Specifically, changing the Val229 residue to alanine, selected in this study for further investigation, was predicted to trigger a change in the cavity and a buried exposure switch at the inactive receptor, thereby potentially modifying the interactions between itself and other pocket residues with cholesterol.

Further detailed investigations of GLP-1R V229A behaviours in beta cells revealed an overall reduction in cholesterol binding under vehicle conditions, which correlated with reduced lateral diffusion, average displacement, and speed of movement across the plasma membrane of the V229A receptor under these conditions. Detailed examination of the receptor oligomerisation state using N&B also demonstrated a greater population of higher order oligomers under vehicle conditions for the V229A *versus* WT GLP-1R. RICS lateral diffusion takes into consideration the movement of molecules in regions of interest within cells (57); the reduced lateral diffusion of GLP-1R V229A could therefore be due to the mutant receptor existing as a subpopulation of pre-clustered, higher order oligomeric assemblies in absence of agonist stimulation, predicted to cause a decrease in the movement of these clusters and potentially hinder cholesterol binding. Interestingly, GLP-1R V229A also presented with a higher tendency to segregate to cholesterol- and sphingolipid-rich flotillin-positive lipid nanodomains, or lipid rafts, in the apo-state, so that the increased clustering of GLP-1R V229A could potentially be triggered by increased mutant receptor partitioning to these lipid nanodomains. This observation also highlights the complexity that modifying a residue within a cholesterol binding site might have on the overall pattern of receptor interactions with cholesterol and other plasma membrane lipids, as increased segregation to cholesterol-rich lipid rafts occurs despite an overall reduction in total cholesterol binding under vehicle conditions observed for the V229A mutant receptor.

GLP-1R V229A receptor pre-clustering under vehicle conditions did not however trigger any measurable changes in the lateral diffusion of the lipid dye Laurdan, which allows for the detection of different plasma membrane organisation states as either liquid ordered or disordered nanodomains (58). Laurdan is a non-species-specific lipid probe that cannot discriminate between different lipids at the plasma membrane so that its lateral diffusion would represent the movement of other lipids besides cholesterol, hence potentially explaining the lack of effect on its lateral diffusion by expression of the mutant *versus* WT receptors. We nevertheless observed, by RICCS analysis, a tendency for reduced co-diffusion of Laurdan with GLP-1R V229A under vehicle conditions, an effect normally only present in stimulated conditions for WT receptor, with no further change after agonist stimulation observed for the V229A mutant, suggesting a different pattern of interaction of V229A *versus* WT GLP-1R with plasma membrane lipids.

Underscoring the importance that direct cholesterol engagement has in the modulation of GLP-1R function, the changes in cholesterol binding and plasma membrane behaviours introduced by the V229A substitution led to significant effects on GLP-1R trafficking and signalling in beta cells: V229A caused a decrease in GLP-1R recruitment to CCPs and receptor internalisation, accompanied by an increase in $G\alpha_s$ (measured with mini-G_s) and β-arrestin 2 engagement, as well as increased plasma membrane recycling following exendin-4 stimulation. Overall, the V229A receptor presented with biased signalling favouring $G\alpha_s$ coupling over β-arrestin 2 recruitment and receptor localisation and activation at the plasma membrane. GLP-1R biased signalling also occurs in WT receptors following activation with modified peptide agonists (59). For example, biased GLP-1R signalling is observed following stimulation with exendin-phe1, which carries a phenylalanine substitution at position 1 of exendin-4, causing a similar reduction in receptor internalisation and increased plasma membrane recycling to GLP-1R V229A (60). In contrast, however, exendin-phe1 triggers essentially no β-arrestin 2 recruitment to the receptor, as well as prolonged GLP-1R-induced cAMP and insulin secretion (60), together with reduced GLP-1R clustering and lipid raft recruitment (31), while GLP-1R V229A presents with increased oligomerisation at vehicle conditions and acute effects on beta cell function (summarised in Figure 9 and Table 1). Some of these effects are in fact analogous to those previously observed by reducing beta cell/islet cholesterol with simvastatin: for example, both manipulations led to a reduction in GLP-1R plasma membrane lateral diffusion under vehicle conditions, as well as acute increases in GLP-1R-induced cAMP and islet insulin secretion responses. Taken together, these results indicate that modulation of direct GLP-1R-cholesterol interactions is a valid strategy to fine-tune beta cell incretin receptor responses, providing a new avenue for further investigation of novel ways to improve GLP-1R signalling outputs.

Assay	**GLP-1R V229A *versus* GLP-1R WT**	
	Vehicle (inactive)	Exendin-4 (active)
Surface expression	≈	N/A
Cholesterol binding	↓	≈
Plasma membrane diffusion	↓↓	≈
Plasma membrane displacement	↓	≈
Plasma membrane speed	↓	≈
Oligomerisation	↑	≈
Lipid raft recruitment	↑	↑
CCP recruitment	≈	↓
Internalisation	N/A	↓
Recycling	N/A	↑
Degradation	N/A	≈
Mini-G_s recruitment	N/A	↑↑
β-arrestin 2 recruitment	N/A	↑
Mini-G_q recruitment	N/A	≈
Activation at plasma membrane	N/A	↑↑
Activation at endosomes	N/A	↑
cAMP	N/A	↑
Insulin secretion	↓ cells / ≈ islets	≈ cells / ↑ islets

Table 1: Overview of effects of GLP-1R V229A in inactive and active states compared with GLP-1R WT. (↑ increased, ↓ decreased, ≈ unchanged).

The phenomenon of cholesterol modification of GPCR outputs by direct receptor binding has been previously demonstrated for other GPCR classes, especially class A GPCRs (61, 62). For example, cholesterol binding sites were identified in the adenosine A_{2A} receptor; mutation of residues within the predicted receptor-cholesterol binding sites caused changes in basal receptor activity, ligand binding, G protein coupling and cAMP responses (21). Receptor-cholesterol interactions were also affected by either agonist or antagonist binding (61). Similarly, determining the effect that different agonists and/or antagonists might have on GLP-1R-cholesterol interactions might also provide further valuable insights into their specific mechanisms of action.

Our results serve as a first for a class B1 GPCR, highlighting the importance of GPCR-lipid interactions on receptor function and dynamics for this receptor class. It further confirms cholesterol binding pockets as high value sites for GLP-1R allosteric modulation, with the capacity to fine-tune GLP-1R trafficking, signalling and functional outputs. Further investigations to fully elucidate the effect of the V229A substitution on GLP-1R-cholesterol interactions might include detailed atomistic MD simulations of WT *versus* V229A receptors, as well as resolving cryo-EM structures of mutant and WT receptors in nanodiscs containing relevant lipid compositions to preserve receptor-lipid interactions in their native environment. Large cgMD simulations including increased numbers of WT or mutant receptors in a membrane environment with varying cholesterol levels could also be performed to determine the effect of cholesterol on GLP-1R oligomerisation. Finally, further high-throughput investigations to evaluate all other key residues involved in GLP-1R-cholesterol binding will generate high value data for the future development of novel GLP-1R allosteric modulators with improved signalling properties for the treatment of T2D and obesity.

Materials and Methods

Animal studies

In vivo studies were carried out under the approval of the UK Home Office Animals (Scientific Procedures) Act 1986 Project Licence PP7151519 (PPL Holder: Dr A. Martinez-Sanchez, Imperial College London) at the Central Biological Services unit of Imperial College London. Animals were housed in individually ventilated cages in groups up to 5 adult mice in a controlled environment (temperature, 21 to 23°C; 12-hour light and 12-hour dark cycles) with free access to standard chow (63) or high-cholesterol diet when relevant.

Intraperitoneal glucose tolerance tests (IPGTTs)

C57BL/6 WT mice were fed a standard chow diet or a rodent diet with 10 kcal% fat and 2% cholesterol (D01101902CR, Research Diets, Inc) for 5 weeks (8-9 female mice per condition). Animals were fasted for 2 hours prior to intraperitoneal injection of glucose (2 g/kg) +/- exendin-4 (1 nmol/kg) and continued to fast for 6 hours when blood glucose levels were assessed from the tail vein using a Contour glucometer (Bayer) and strips at 0-, 10-, 30-, and 60-minute time-points, with glucose response curves generated from these data.

Mouse pancreatic islet isolation and culture

Islets were isolated from mice pancreata previously infused with RPMI-1640 medium, (21875091, Thermo Fisher Scientific) containing 1 mg/mL collagenase (*Clostridium*

histolyticum) (S1745602, Nordmark Biochemicals), dissected, and incubated in a 37°C water bath for 10 minutes to digest the tissue. RPMI-1640 medium with 10% foetal bovine serum (FBS) (F7524, Sigma Aldrich) was added and mixed vigorously for 20 seconds to stop the reaction. The dissected pancreata were subsequently washed in RPMI-1640 medium prior to islet separation using a gradient with Histopaque-1119 and -1083 (both from Sigma Aldrich). Isolated islets were transferred to non-adherent dishes containing RPMI-1640 medium with 2 mM L-glutamine and 11 mM D-glucose supplemented with 10% FBS and 1% penicillin/streptomycin (p/s) (P4458, Sigma Aldrich) in a humidified incubator at 37°C and 5% CO_2. Islets were allowed to recover for 24 hours prior to use (63).

Cholesterol modification treatments

To increase cholesterol, islets isolated from chow-fed C57BL/6 WT mice were pre-incubated in 20 mM cholesterol loaded onto methyl-β-cyclodextrin (MβCD) (C4951, Sigma Aldrich) diluted in 1X Krebs-Ringer bicarbonate-Hepes (KRBH) buffer [140 mM NaCl, 3.6 mM KCl, 1.5 mM $CaCl_2$, 0.5 mM $MgSO_4$, 0.5 mM NaH_2PO_4, 2 mM $NaHCO_3$, 10 mM Hepes, saturated with 95% O_2 / 5% CO_2; pH 7.4 and 0.1% bovine serum albumin (BSA)] for 1 hour at 37°C prior to assays being carried out. Control islets were pre-incubated in KRBH buffer alone. For reduced cholesterol, islets were pre-incubated in 10 µM simvastatin (S6196, Sigma Aldrich) diluted in RPMI-1640 supplemented with 10% lipoprotein deficient serum (LPDS) (S5394, Sigma Aldrich) and 1% p/s for a minimum of 18 hours prior to the assays. Control islets were pre-incubated in RPMI-1640 supplemented with 10% FBS and 1% p/s for the same time.

Assessment of cholesterol levels

Islet were washed once with PBS and cholesterol labelled according to the Cholesterol Assay kit (cell-based) (ab133116, Abcam). Briefly, islets were fixed for 15 minutes with the cell-based assay Fixative solution. Islets were then washed with the Cholesterol Detection wash buffer, incubated for a minimum of 1 hour in Filipin III diluted in the Cholesterol Detection Assay buffer, and washed again in wash buffer before immediate imaging on a Zeiss LSM-780 inverted confocal laser-scanning microscope from the Facility for Imaging by Light Microscopy (FILM) at Imperial College London, with a 63X objective and a laser excitation wavelength of 340-380 nm and emission of 385-470 nm. Raw fluorescence images were analysed using Fiji to determine the average fluorescent intensity representing the level of cholesterol per islet.

Cell culture

INS-1 832/3 cells, a rat insulinoma subline with preserved incretin responses (64), and derivative INS-1 832/3 cells with endogenous rat GLP-1R deleted by CRISPR/Cas9 [INS-1 832/3 GLP-1R KO (27)], were grown in RPMI-1640 medium with 2 mM L-glutamine and 11 mM D-glucose, supplemented with 10% FBS, 1% p/s, 10 mM HEPES solution (H3537, Sigma-Aldrich), 1 mM sodium pyruvate (11360070, Thermo Fisher Scientific) and 0.05 mM β-mercaptoethanol (M3148, Sigma Aldrich) in a humidified incubator at 37°C and 5% CO_2. INS-1 832/3 SNAP/FLAG-hGLP-1R WT and V229A cells were generated in house from INS-1 832/3 GLP-1R KO cells following transfection with pSNAP/FLAG-hGLP-1R (Cisbio) or pSNAP/FLAG-hGLP-1R-V229A (generated *in house* by site-directed mutagenesis, see below), followed by selection with 1 mg/mL G418 sulphate (A1720, Sigma Aldrich). Cells were labelled with SNAP-Surface Alexa Fluor 546 (New England Biolabs) and SNAP-expressing

fluorescent cells sorted by fluorescence-activated cell sorting (FACS) and maintained as above with media supplemented with 0.5 mg/mL G418.

cAMP live imaging

cAMP cADDis biosensor imaging

INS-1 832/3 SNAP/FLAG-hGLP-1R WT *versus* V229A cells seeded onto glass bottom MatTek dishes, or pancreatic islets, were transduced overnight with the Green Up cADDis biosensor in a BacMam vector (#U0200G, Montana Molecular), according to the manufacturer's instructions. Cells were washed and imaged in RPMI without phenol red, while islets were washed and encased in Matrigel (Corning) and imaged in KRBH buffer supplemented with 6 mM glucose. Green fluorescence was recorded at 6 second intervals in a 20X objective 37°C heated stage Nikon spinning disk field scanning confocal microscope. A baseline reading was taken for 1 minute, then 100 nM exendin-4 was added and cells/islets imaged for a further 5 minutes, prior to addition of 100 µM isobutyl methylxanthine (IBMX) + 10 µM forskolin (FSK) and 2-minute imaging for maximal response. Fluorescent intensity per islet or cell was calculated using Fiji and responses plotted relative to the baseline period. Area under the curve (AUC) was calculated for the exendin-4 period using GraphPad Prism 10.

cAMP $^{T}EPAC^{VV}$ Fluorescence Resonance Energy Transfer (FRET) imaging

Islets extracted from Pdx1$^{Cre\text{-}ERT}$-CAMPER mice, conditionally expressing the $^{T}EPAC^{VV}$ cAMP biosensor in beta cells under the control of the *Pdx1* promoter conjugated to a mutant oestrogen receptor sequence (63), were incubated in 1 µM 4-hydroxytamoxifen for 24 hours to induce $^{T}EPAC^{VV}$ expression, treated with simvastatin as above, washed, encased in Matrigel and imaged in 6 mM glucose KRBH buffer using a Zeiss LSM-780 inverted confocal laser-scanning microscope in a 20X objective at 37°C. FRET between the Turquoise donor and the Venus acceptor within $^{T}EPAC^{VV}$ was recorded every 6 seconds. A baseline reading was taken for 1 minute, followed by a 5-minute recording period with 100 nM exendin-4. Glucose was then increased to 16 mM and islets imaged for a further 3 minutes before addition of 100 µM IBMX + 10 µM FSK as above to record maximal responses. Fluorescent intensities for Turquoise and Venus channels were extracted per islet in Fiji and Turquoise/Venus ratio calculated corresponding to cAMP levels. Responses were presented as average intensity traces per islet relative to its baseline period, and AUC calculated as above.

Insulin secretion assays

Insulin secretions in islets

Purified islets were incubated in 3 mM glucose KRBH buffer for 1 hour at a shaking water bath at 37°C. Islets were then incubated in 11 mM glucose KRBH buffer +/- 100 nM exendin-4 for 30 minutes. Supernatants containing secreted insulin were collected, spun at 1,000 rpm for 1 minute and transferred to new Eppendorf tubes. Islets were then lysed using acidic ethanol (75% ethanol, 15 mM HCl), sonicated 3X 10 seconds and centrifuged at 1,000 rpm for 3 minutes, and supernatants collected to assess internal insulin content and stored at -20°C. Each condition was analysed in triplicate with 10 islets per replicate.

Insulin secretions in cells

INS-1 832/3 SNAP/FLAG-hGLP-1R WT or V229A cells were seeded onto 48-well plates, pre-incubated in 3 mM glucose media overnight, washed with KRBH buffer and incubated in 3 mM glucose KRBH buffer for 1 hour before stimulation with 11 mM glucose KRBH +/- 100 nM exendin-4 for 1 hour. Supernatants containing secreted insulin were collected and spun at 1,000 rpm for 3 minutes and stored at -20°C. Cells were lysed with lysis buffer (KRBH supplemented with 0.1% BSA and 1% Triton X-100), collected in an Eppendorf tube, sonicated 3X 10 seconds and centrifuged at 13,000 rpm for 10 minutes. Supernatants containing internal insulin were collected to determine total insulin content. Samples were stored at -20°C until they were analysed.

Insulin concentrations from cells and islets were determined using the Insulin Ultra-Sensitive HTRF Assay Kit (2IN2PEG, Cisbio) according to the manufacturer's instructions. Standard curves were generated using GraphPad Prism 10 and insulin concentration for each sample interpolated from the standard curve. Percentage of insulin secreted was determined from the secreted over the total (internal + secreted) insulin concentrations.

Coarse-grained molecular dynamics (cgMD) simulations

The structure of GLP-1R in inactive form was adopted from GPCRdb (65), using refined GLP1R model PDB ID: 6LN2 (55, 66). The active form was adopted from cryoEM structure PDB ID: 6x18 (53) with the missing loop modelled back in using MODELLER version 10.4 (67). The GLP-1R was coarse-grained using Martinize2 (68) with MARTINI 3 forcefield (69). The ElNeDyn elastic network restraint was applied to active and inactive GLP-1R using an elastic bond force constant of 500 kJ/mol/nm^2 and an upper cut-off of 0.9 nm (70). The transmembrane region of GLP-1R was predicted using PPM 3.0 Web Server (71) and embedded into an asymmetric lipid membrane bilayer in a 18x18x17 nm^3 box using insane.py (72), with lipid composition as follows: POPC (30%), DOPC (30%), POPE (8%), DOPE (7%) and cholesterol (25%) in the outer leaflet and POPC (5%), DOPC (5%), POPE (20%), DOPE (20%), POPS (8%), DOPS (7%), PIP_2 (10%) and cholesterol (10%) in the inner leaflet. Mammalian plasma membrane composition was adopted from Song *et al* (73). The new MARTINI 3 lipid model for cholesterol was used in this study (74, 75). Each system was solvated using MARTINI water (69) and 150 nM NaCl, followed by the standard minimisation and equilibration protocols from CHARMM-GUI Martini Marker (76). The production simulation was 10 µsec in length and was repeated 3X. The v-rescale thermostat (tau 1.0 psec) (77) and the Parrinello–Rahman barostat (tau 12.0 psec) (78) were used to maintain temperature (303.15 K) and pressure (1 bar) on all production runs. All simulations were done using GROMACS 2022.4 (79). Cholesterol interaction profiles were calculated using PyLipID (29) with a cut-off of 0.7 nm. Trajectory was analysed using gromacs tool and VMD (80).

Site-directed mutagenesis of GLP-1R cholesterol binding sites

Human SNAP/FLAG-tagged GLP-1R (SNAP/FLAG-hGLP-1R) (Cisbio) was used as the template to generate GLP-1R cholesterol binding mutants for screening. Site-directed mutagenesis primers (Table 2) were designed to replace the relevant amino acid residue with alanine and carried out using the PfuUltra II Fusion HS DNA Polymerase kit (600670, Agilent) according to the manufacturer's instructions. PCR products were treated with 1 µL Dpn1 (10 U/µL) for 1 hour at 37°C to digest parental DNA. Digested DNA samples were transformed into NEB10-beta Competent *E. coli* High Efficiency cells (C3019H, New England Biolabs)

according to the manufacturer's instructions. Mutant plasmids were sent for Sanger sequencing (Azenta/Genewiz) to confirm the amino acid change to alanine.

GLP-1R cholesterol binding mutant	Forward primer (5'-3')	Reverse primer (5'-3')	Side chain charge change
BATCH 1 SCREEN			
I323A	CATTGGGGTGAACTTCCTCGCCTTTGTTCGGGTCATCTGC	GCAGATGACCCGAACAAAGGCGAGGAAGTTCACCCCAATG	non-polar to non-polar
S163A	CTCTGGTTATCGCCGCTGCGATCCTCCTC	GAGGAGGATCGCAGCGGCGATAACCAGAG	polar to non-polar
S225A	CCAGGACTCTCTGGCCTGCCGCCTGGTG	CACCAGGCGGCAGGCCAGAGAGTCCTGG	polar to non-polar
V229A	GAGCTGCCGCCTGGCGTTTCTGCTCATGC	GCATGAGCAGAAACGCCAGGCGGCAGCTC	non-polar to non-polar
BATCH 2 SCREEN			
L167A	CCTCTGCGATCCTCGCCGGCTTCAGACACC	GGTGTCTGAAGCCGGCGAGGATCGCAGAGG	non-polar to non-polar
V160A	CCTTCTCTGCTCTGGCTATCGCCTCTGCGAT	ATCGCAGAGGCGATAGCCAGAGCAGAGAAGG	non-polar to non-polar
I165A	GTTATCGCCTCTGCGGCCCTCCTCGGCTTCAG	CTGAAGCCGAGGAGGGCCGCAGAGGCGATAAC	non-polar to non-polar
G151A	CATCTACACGGTGGCCTACGCACTCTCCT	AGGAGAGTGCGTAGGCCACCGTGTAGATG	non-polar to non-polar
BATCH 3 SCREEN			
D372A	GCCTTTGTGATGGCCGAGCACGCCCGG	CCGGGCGTGCTCGGCCATCACAAAGGC	acidic to non-polar
H363A	CATCCCCCTGCTGGGGACTGCTGAGGTCATCTTTG	CAAAGATGACCTCAGCAGTCCCCAGCAGGGGGATG	basic to non-polar
L401A	AGGGGCTGATGGTGGCCATAGCATACTGCTTTGTCAACAAT	ATTGTTGACAAAGCAGTATGCTATGGCCACCATCAGCCCCT	non-polar to non-polar
I400A	CAGGGGCTGATGGTGGCCGCATTATACTGCTTTGTCAAC	GTTGACAAAGCAGTATAATGCGGCCACCATCAGCCCCTG	non-polar to non-polar

Table 2: Site-directed mutagenesis primers for SNAP/FLAG-hGLP-1R cholesterol binding mutant generation.

GLP-1R surface expression and internalisation by confocal microscopy

INS-1 832/3 GLP-1R KO cells were transiently transfected with SNAP/FLAG-hGLP-1R WT or cholesterol-binding mutants; purified GLP-1R KO mouse islets were transduced with SNAP/FLAG-hGLP-1R WT *versus* V229A adenoviruses (generated by VectorBuilder) at an MOI of 1. Cells or islets were incubated for 24 hours post-transfection / transduction before labelling with 1 μM SNAP-Surface fluorescent probes (New England Biolabs) for 15-20 minutes for cells, or 7 minutes for islets, in full media at 37°C. Cells were washed and imaged in RPMI-1640 without phenol red (32404014, Thermo Fisher Scientific), while islets were

washed and imaged in 6 mM glucose KRBH buffer using a Nikon spinning disk field scanning confocal microscope with a 60X oil objective at 37°C. Cells were imaged by time-lapse microscopy with images taken every 6 seconds; a baseline recording was taken for 1 minute before addition of 100 nM exendin-4 and further imaging for 10 minutes. Islets were imaged in vehicle conditions or 5 minutes after stimulation with 100 nM exendin-4 at 37°C.

Raw images were analysed using Fiji and the full width half maximum (FWHM) of a line profile macro, developed by Steven Rothery, FILM Facility, Imperial College London, employed to determine the change in SNAP fluorescence intensity at the plasma membrane from individual cells. SNAP/FLAG-hGLP-1R surface expression levels were determined from the average intensity during the baseline period for cells or from the vehicle images for islets. Receptor internalisation was calculated from the loss of fluorescence intensity at the plasma membrane after 10 minutes of exendin-4 stimulation compared to baseline intensity for cells, or from the loss of fluorescence intensity after 5 minutes of exendin-4 stimulation *versus* vehicle for islets.

PhotoClick cholesterol binding assay

PhotoClick cholesterol (37.5 nmoles, 700147P, Avanti Polar Lipids) was agitated in 2 mM MβCD in Hanks Balanced Salt Solution (HBSS) (14025092, Thermo Fisher Scientific) overnight at room temperature to facilitate intracellular delivery. INS-1 832/3 SNAP/FLAG-hGLP-1R WT or V229A cells were seeded onto 6-well plates and incubated in 18.75 nmoles of PhotoClick cholesterol loaded onto MβCD in HBSS for 1 hour at 37°C protected from light. Cells were then stimulated with 100 nM exendin-4 or vehicle for 2 minutes, washed with ice cold PBS and UV irradiated at 365 nm with a UV Crosslinker for 5 minutes in ice cold PBS to activate the photoreactive diazirine group in the PhotoClick cholesterol. Cells were then lysed in 1X TBS (50 mM Tris-HCl, 150 mM NaCl, pH 7.4) supplemented with 1 mM EDTA, 1% Triton X-100, phosphatase inhibitor cocktail (P5726, Sigma Aldrich), and protease inhibitor cocktail (11873580001, Roche Diagnostics). Lysates were sonicated 3X 10 seconds, centrifuged at 10,000 rpm for 10 minutes and incubated with anti-FLAG M2 affinity gel (A2220, Sigma Aldrich) rotating overnight at 4°C to immunoprecipitate the SNAP/FLAG-hGLP-1R. Following immunoprecipitation, the bead-bound SNAP/FLAG-hGLP-1R was incubated with a click chemistry mix (20 μM rhodamine-azide, 1 mM TCEP, 100 μM TBTA, 1 mM $CuSO_4$) for 1 hour at room temperature gently agitating to fluorescently label the PhotoClick cholesterol. Urea buffer (2X) was added in a 1:1 ratio and samples incubated for 10 minutes at 37°C prior to 10% SDS-PAGE gel separation and imaging using a ChemiDoc MP imaging system to detect fluorescently labelled cholesterol. The proteins were then transferred onto a PVDF membrane and corresponding SNAP/FLAG-hGLP-1R levels detected by Western blotting with an anti-SNAP antibody (P9310S, New England Biolabs). Data was represented as amount of bound Photo-Click cholesterol relative to SNAP/FLAG-hGLP-1R.

GST-D4H*-mCherry purification

pGEX-KG-D4H*-mCherry plasmid (Addgene #134604) was used to purify D4H*-mCherry as previously described (32). Briefly, a plasmid colony was grown in 5 mL LB broth overnight at 37°C. Culture was scaled up into a 1 L flask and grown for a further 4 hours, and protein production induced with 0.5 mM IPTG for 4 hours. Bacterial culture was pelleted at 2,500 rpm for 30 minutes and resuspended in lysis buffer (0.1 M NaCl, 20 mM Tris-HCl, pH 8.0, 1 mM DTT, 1X protease inhibitor cocktail) and 0.35 mg/mL lysozyme added for 30 minutes on ice. Samples were sonicated at 50% Amp for 10 seconds and 10 seconds break for a total of 4

minutes. 1% Triton X-100 was added, and samples rocked at 4°C for 30 minutes before centrifugation and incubation of supernatants with glutathione beads (GE17-0756-01, Sigma Aldrich) for 2 hours rocking at room temperature to capture the GST-D4H*-mCherry protein. D4H*-mCherry protein was eluted in elution buffer (25 mM L-glutathione, 50 mM Tris-HCl pH 8.8, 200 mM NaCl), filtered through a 30 kDa centrifugal filter unit (UFC203024, Thermo Fisher Scientific) and stored at -80°C.

D4H*-mCherry cell labelling and imaging

INS-1 832/3 SNAP/FLAG-hGLP-1R WT or V229A cells were seeded onto 13-mm coverslips and labelled with SNAP-Surface 488 probe in full media for 20 minutes before stimulation with 100 nM exendin-4 for 2 minutes at 37°C. Cells were washed with PBS and fixed with 4% paraformaldehyde (PFA) for 10 minutes at 4°C, permeabilised for 15 seconds in a liquid nitrogen bath, blocked in 1% BSA / PBS for 1 hour at room temperature, incubated with D4H*-mCherry (1:25 in 1% BSA / PBS) for 2 hours, washed with PBS and post-fixed in 4% PFA for 10 minutes at room temperature. Coverslips were washed, mounted onto microscope slides using ProLong™ Diamond Antifade Mountant with DAPI (P36966, Thermo Fisher Scientific) and imaged with a 63X oil objective Leica Stellaris 8 inverted confocal microscope from the FILM facility at Imperial College London. Raw images were analysed in Fiji using the Coloc 2 plugin to determine SNAP/FLAG-hGLP-1R co-localisation with D4H*-mCherry.

Raster Image Correlation Spectroscopy (RICS) image capture and analysis

INS-1 832/3 SNAP/FLAG-hGLP-1R WT or V229A cells were seeded onto glass bottom MatTek dishes and labelled with SNAP-Surface 647 (S9136S, New England Biolabs) for 15 minutes at 37°C in full media, washed and imaged in RMPI-1640 media without phenol red using a 100X oil objective on a Leica Stellaris 8 STED FALCON microscope from the FILM Facility at Imperial College London using confocal settings as previously described (81). Images were analysed as previously described (82, 83). Briefly, cells were imaged at the basal plasma membrane under vehicle conditions and following stimulation with 100 nM exendin-4 with a format size of 256x256 pixels and 80 nm pixel size for 200 consecutive frames. RICS analysis was carried out to determine the diffusion coefficient of WT *versus* V229A GLP-1R in vehicle and stimulated conditions using the SimFCS 4 Software (Global Software, G-SOFT Inc.). Three different regions of interest of size 32x32 pixels for each image and a moving average of 10 was applied to avoid any artefacts due to cellular motion or very slow-moving particles. Average intensity, intensity plots, 2D autocorrelation maps and 3D autocorrelation fits were generated for each condition and cell line investigated (84, 85).

GLP-1R Total Internal Reflection Fluorescence (TIRF)-single particle tracking (SPT)

INS-1 832/3 GLP-1R KO cells were transiently transfected with WT or V229A human GLP-1R-monomeric EGFP fusion constructs, generated *in house* by mutating EGFP Ala207 to Lys in hGLP-1R-EGFP [kind gift from Dr Alessandro Bisello (86)] using the following primers: Forward (5' to 3'): CCTGAGCACCCAGTCCAAGCTGAGCAAAGACCCCA and Reverse (5' to 3'): TGGGGTCTTTGCTCAGCTTGGACTGGGTGCTCAGG, and WT hGLP-1R-mEGFP to V229A with the primers from Table 2. Transfected cells were seeded onto glass bottom MatTek dishes, imaged live at 37°C in RPMI-1640 without phenol red under vehicle conditions or following stimulation with 1 μM exendin-4 and images analysed as previously described (87) with some changes. Cells were imaged in a Nikon spinning disk field scanning confocal

microscope using a 100X oil objective under TIRF illumination with the following microscope settings using the MetaMorph software: 488 nm excitation laser, exposure time of 150 msec, 10% laser power at a rate of 1 frame per second for 150 frames. Images were loaded onto the Icy software; an ROI was drawn around each cell and Spot Detector used to determine the spots in each image. A scale of 2 with a sensitivity of 70 was used and kept constant for each experiment. Spot Tracking followed by Track Manager were used to determine the speed and displacement for each particle detected in the plasma membrane of cells.

Raster Image Cross-Correlation Spectroscopy (RICCS) with Number and Brightness (N&B) image acquisition and data processing

INS-1 832/3 SNAP/FLAG-hGLP-1R WT or V229A cells were seeded onto μ-Slide 8-well glass bottom microscope plates (Ibidi) and labelled with SNAP-Surface Alexa Fluor 647 for 10 minutes followed by Laurdan (6-dodecanoyl-2-(dimethylamino) naphthalene), an environmentally sensitive plasma membrane lipid dye (34), for 5 minutes prior to imaging. Cells were washed with PBS and imaged in RMPI 1640 medium without phenol red using the confocal settings of a Leica Stellaris 8 STED FALCON in an 86X objective and a 10% power 405 nm excitation laser and emission ranges of 415-465 nm and 470-520 nm for Laurdan, plus a 5% power 647 nm excitation laser for SNAP-Surface Alexa Fluor 647. Two hundred consecutive frames were captured for 2.45 minutes at a pixel size of 80 nm and a format size of 256x256 pixels. Cells were imaged under vehicle conditions and after stimulation with 100 nM exendin-4. Further analysis was carried out using the SimFCS 4 Software to determine the RICCS cross-correlation between Laurdan and SNAP/FLAG-hGLP-1R. Specifically, Ch2-Ch1 (B1-B2 map) RICS analysis of brightness (intensity of fluorescence signal) in one channel cross-correlates with brightness in the second channel, allowing for the calculation of cross-correlation. N&B analysis was performed from the SNAP signal to determine the oligomerisation of SNAP/FLAG-hGLP-1R after exendin-4 stimulation by assessing the apparent brightness and number of pixels involved using SimFCS 4 software. Three different regions of interest of size 64x64 pixels per image and a moving average of 10 was applied to avoid any artefacts due to cellular motion or very slow-moving particles.

GLP-1R Time-Resolved FRET (TR-FRET) conformational assay

INS-1 832/3 SNAP/FLAG-hGLP-1R WT or V229A cells were labelled with 40 nM SNAP-Lumi4-Tb (SSNPTBC, Cisbio), a lanthanide fluorophore probe for TR-FRET, for 1 hour at 37°C in full media. Cells were washed with HBSS and resuspended in 60 nM NR12A, a solvatochromic photostable plasma membrane lipid probe (88) in HBSS, incubated for 5 minutes, and seeded onto a white opaque 96-well half-area plate. TR-FRET was carried out as described (89). Briefly, a baseline reading was taken for 5 minutes using a Flexstation 3 plate reader with excitation wavelength of 335 nm, and emissions of 490 nm and 590 nm. The cells were then stimulated with 100 nM exendin-4, or vehicle, and the plate read for a further 20 minutes. Receptor conformational shift was calculated as the 590/490 ratio of both wavelength emission signals after normalising to basal signal under vehicle conditions. AUC was calculated and used for statistical analysis.

Lipid raft recruitment assay

INS-1 832/3 SNAP/FLAG-hGLP-1R WT or V229A cells were seeded onto 6-cm dishes and stimulated with 100 nM exendin-4 or vehicle for 2 minutes at 37°C, placed on ice, and washed

with ice cold PBS before being osmotically lysed with 20 mM Tris-HCl (pH 7.0) supplemented with protease and phosphatase inhibitor cocktails. The cell suspension was homogenized by passing through a 21-gauge needle and ultracentrifuged for 1 hour at 41,000 rpm at 4°C. The supernatant was discarded, and the pellet resuspended in cold PBS + 1% Triton X-100 plus protease and phosphatase inhibitor cocktails, transferred to an Eppendorf tube and allowed to rotate for 30 minutes at 4°C. The suspension was then ultracentrifuged for another hour at 41,000 rpm at 4°C to separate detergent-resistant (DRM) from detergent-soluble (DSM) membrane fractions: the 'disordered' DSM fraction in the supernatant was retained for analysis and the 'ordered' DRM (lipid raft) fraction was resuspended in 1% SDS plus protease and phosphatase inhibitor cocktails, sonicated, centrifuged for 10 minutes at 13,500 rpm at 4°C, and analysed via SDS-PAGE and Western blotting as in (25). Blotted membranes were analysed using Fiji and SNAP levels normalised to flotillin used as DRM loading control.

GLP-1R co-localisation with clathrin-coated pits (CCPs) with using TIRF microscopy

INS-1 832/3 SNAP/FLAG-hGLP-1R WT or V229A cells were transfected with clathrin light chain (CLC)-GFP and plated onto poly-L-lysine-coated glass coverslips. Prior to imaging, cells were labelled at 37°C with 5 µM SNAP-Surface 549 probe for 30 minutes in full media and washed. Microscopy was performed on a custom-built TIRF microscope based on a Zeiss Axiovert 135 with DPSS lasers at 405, 491 and 561 nm, 100X/1.45 NA objective. Colour channels were split using a Dualview (Optical Insights) and projected side by side onto an EMCCD camera (QuantEM:512SC, Photometrics). Still images were acquired by sequential excitation with the 473 and 561 nm lasers. During the experiments, cells were incubated in an imaging solution containing 138 mM NaCl, 5.6 mM KCl, 2.6 mM $CaCl_2$, 1.2 mM $MgCl_2$, 3 mM glucose and 5 mM HEPES, pH 7.4 at ~35°C. Exendin-4 (100 nM) was added for at least 10 minutes to trigger receptor endocytosis. Calibration and alignment were performed using 100 nm polystyrene beads (Molecular Probes). To quantify SNAP/FLAG-hGLP-1R association with clathrin, circular ROIs surrounding individual well defined puncta of fluorescence (5-50 per cell) were selected on CLC-GFP images and transferred to the corresponding SNAP ones using a Fiji macro and average fluorescence per pixel was measured in a central circle (c) of diameter 5 pixels (0.55 µm) at each puncta location, in a surrounding annulus (a) with an outer diameter of 7 pixels (0.77 µm), and in an area not containing any cell as background (bg). The specific cluster-associated fluorescence ΔF was calculated by subtracting the annulus value from that of the circle ($\Delta F = c-a$). Local fluorescence from CLC-GFP molecules not associated with the cluster site was calculated by subtracting the background from the annulus value ($S = a-bg$) and used to normalize ΔF to the expression level of the tested protein (90). The reported parameter $\Delta F/S$ can be interpreted as the GLP-1R affinity for clathrin structures.

GLP-1R trafficking by high content microscopy

SNAP/FLAG-hGLP-1R internalisation

INS-1 832/3 SNAP/FLAG-hGLP-1R WT or V229A cells were seeded onto poly-L-lysine-coated black, clear bottom 96-well plates. Cells were imaged and analysed as previously described (91). Briefly, cells were labelled with 1 µM BG-S-S-649, a cleavable SNAP-Surface probe, in full media for 30 minutes at 37°C, washed with PBS and stimulated with vehicle or 100 nM exendin-4 in reverse time order for 30, 15, 10 and 5 minutes at 37°C in full media. Cells were washed with ice cold HBSS, and the following steps performed at 4°C. Surface receptor probe was cleaved by incubation in 100 mM 2-mercaptoethane-sulfonic acid sodium salt (Mesna) in

1X TAE buffer, pH 8.6 or incubated 1X TAE buffer alone for 5 minutes and then washed and imaged in HBSS using a custom-written high content analysis software in Micro-Manager in a Cairn Research widefield microscope with Nikon Ti2, CoolLED light source and 20X phase contrast objective for both epifluorescence and transmitted phase contrast with 9 ROI acquired per well. Phase contrast images, analysed using PHANTAST in Fiji, were used to determine the cell containing region, and BaSiC was used for illumination correction of fluorescent images. Mean intensity for the cell containing region was determined using a custom macro by Steven Rothery, Imperial College London FILM Facility. SNAP/FLAG-hGLP-1R internalisation was calculated by first subtracting non-specific signal of wells treated with Mesna without agonist from all the other wells, then normalising to signal of cells with no Mesna exposure (92).

SNAP/FLAG-hGLP-1R plasma membrane recycling

INS-1 832/3 SNAP/FLAG-hGLP-1R WT or V229A cells were seeded onto poly-L-lysine-coated black, clear bottom 96-well plates in full media, stimulated with vehicle or 100 nM exendin-4 for 1 hour at 37°C to enable receptor internalisation, washed with PBS and incubated in 100 nM tetramethylrhodamine (TMR)-tagged exendin-4 (Ex-4-TMR) in full media for 1 hour or 3 hours at 37°C to label any receptors that recycle back to the plasma membrane after agonist-mediated internalisation. Cells were washed, imaged in HBSS and processed as above with Ex-4-TMR fluorescence signal corresponding to plasma membrane recycled receptor along with low signals of residual surface receptor (83). Background / non-specific fluorescence from wells not treated with Ex-4-TMR was subtracted from all wells followed by normalising to signal from wells not treated with exendin-4 (vehicle conditions).

SNAP/FLAG-hGLP-1R plasma membrane degradation

INS-1 832/3 SNAP/FLAG-hGLP-1R WT or V229A cells were seeded onto poly-L-lysine-coated black, clear bottom 96-well plates in full media and treated as previously described (28). Briefly, cells were washed with PBS and changed to media with no serum + 50 µg/mL cycloheximide to inhibit protein synthesis for 1 hour, then stimulated with vehicle or 100 nM exendin-4 in reverse time order for 8, 6, 4, 2 and 1 hours. Media was changed in the last 30 minutes to full media with vehicle or agonist and 1 µM BG-OG, a permeable SNAP-tag probe to label total residual SNAP/FLAG-hGLP-1R. Cells were washed and imaged in HBSS as above. SNAP/FLAG-hGLP-1R degradation is quantified as the inverse of total residual receptor signal normalised to non-stimulated wells after subtracting non-labelled background signal.

NanoBiT complementation assays

GLP-1R-SmBiT WT was previously cloned *in house* as described in (28). GLP-1R-SmBiT V229A was generated from the WT template by site-directed mutagenesis using the following primers: Forward (5' to 3'): TCTTTCCTGTCGACTCGCGTTTCTGCTTATGCAGT, Reverse (5' to 3'): ACTGCATAAGCAGAAACGCGAGTCGACAGGAAAG. LgBiT-mini-G_s and -mini-G_q were a gift from Prof. Nevin Lambert, Medical College of Georgia, USA, and LgBiT-β-arrestin 2 was purchased from Promega (plasmid no. CS1603B118). For recruitment assays, INS-1 832/3 GLP-1R KO cells were seeded onto 6-well plates and transiently transfected with a combination of 1 µg GLP-1R-SmBiT WT or V229A and either 1 µg of LgBiT-mini-G_s, -mini-G_q or -β-arrestin 2.

Nanobody37 (Nb37) bystander NanoBiT assay was carried out as previously described (28). The constructs required to determine plasma membrane (KRAS CAAX motif), or endosomal (Endofin FYVE domain) GLP-1R activity were a gift from Prof. Asuka Inoue, Tohoku University, Japan. INS-1 832/3 GLP-1R KO cells were seeded onto 12-well plates and transfected as detailed in Table 3.

LgBiT-KRAS CAAX motif (SSSGGGKKKKKKSKTKCVIM)		**Endofin FYVE domain-LgBiT (amino acid region Gln739-Lys806)**	
Plasmid	Concentration	Plasmid	Concentration
SNAP/FLAG-hGLP-1R WT or V229A	0.1 µg	SNAP/FLAG-hGLP-1R WT or V229A	0.1 µg
Nb37-SmBiT	0.05 µg	Nb37-SmBiT	0.25 µg
LgBiT-CAAX	0.05 µg	Endofin-LgBiT	0.25 µg
$G\alpha_s$ (human, short isoform)	0.25 µg	$G\alpha_s$ (human, short isoform)	0.25 µg
Gβ1 (human)	0.25 µg	Gβ1 (human)	0.25 µg
Gγ1 (human)	0.25 µg	Gγ1 (human)	0.25 µg
RIC8B (human, isoform 2)	0.05 µg	RIC8B (human, isoform 2)	0.05 µg
pcDNA 3.1	0.40 µg	pcDNA 3.1	-

Table 3: Transfected plasmid amounts for Nb37 bystander NanoBiT assays.

NanoBiT assays were carried out as previously described (28): 24 hours after transfection, cells were incubated in 3 mM glucose for a minimum of 2 hours, detached and resuspended in NanoGlo Live cell substrate (N2012, Promega), 1:20 dilution in HBSS, and seeded onto an opaque white 96-well half-area plate. Using a Flexstation 3 plate reader, a baseline luminescence reading was acquired for 8 minutes at 37°C, followed by stimulation with vehicle or 100 nM exendin-4 for Nb37 bystander assay, or with serial dilutions of exendin-4 starting from 1 µM, 100 nM, 10 nM to 1 nM for 30 minutes for the mini-G_s / mini-G_q / β-arrestin 2 recruitment assays. Results were normalised to individual basal signal followed by average vehicle responses. Non-linear fit curves of the AUCs were used to generate dose responses using GraphPad Prism 10.

Statistical analyses

All data analyses and graph generation were performed using GraphPad Prism 10 and presented as mean ± standard error of the mean (SEM). Statistical analyses were performed with the tests indicated in the figure legend. Data was deemed significant at $p \leq 0.05$.

Acknowledgements

The authors thank the FILM Facility, Imperial College London for technical support on microscopy experiments and microscopy data analysis, and Prof Mark Sansom and Dr Wanling Song, Dept Biochemistry, University of Oxford, for assistance with the use of PyLipID for the GLP-1R-cholesterol binding site analysis. The A.T. group is funded by grants from Diabetes UK (19/0006094), the MRC (MR/X021467/1), and the Wellcome Trust (301619/Z/23/Z), the latter in collaboration with S.L.R, B.J. and J.B.S; A.I.O. is supported by a PhD Scholarship from the Commonwealth. The S.L.R. group is supported by MRC grant

MR/T017961/1. The S.B. group is supported by the Swedish Research Council, Diabetes Wellness Sweden, Novo Nordisk Foundation, and the Swedish Diabetes Foundation. The J.B.S. lab acknowledges funding from BBSRC (BB/V019791/1) and MRC (MR/W024985/1). B.J. is supported by MRC Clinician Scientist Fellowship MR/Y00132X/1, and by project grants from the MRC and Diabetes UK. The Section of Endocrinology at Imperial College London is funded by grants from the MRC, NIHR and is supported by the NIHR Biomedical Research Centre Funding Scheme and the NIHR/Imperial Clinical Research Facility. The views expressed are those of the author(s) and not necessarily those of the NHS, the NIHR or the Department of Health.

Figure Legends

Figure 1: Effect of changes in cholesterol on GLP-1R agonist responses *in vivo* and in primary islets. (**A**) IPGTTs 6 hours post-intraperitoneal administration of vehicle (Veh) or 1 nmol/kg exendin-4 (Ex-4) in mice fed a chow *vs* 2% cholesterol (high chol) diet for 5 weeks; n = 8-9 female mice per diet. (**B**) Area under the curve (AUC) for glucose curves from (A). (**C**) Ex-4 over Veh glucose levels in chow *vs* 2% cholesterol diet fed mice. (**D**) Average intensity of filipin staining (to label cholesterol) in mouse islets preincubated with Veh or MβCD loaded with 20 mM cholesterol (MβCD/chol) for 1 hour; n = 5 islet preps from separate mice; representative islet images also shown; size bars, 10 μm. (**E**) Percentage of insulin secretion from mouse islets preincubated with Veh or MβCD/chol before stimulation with 11 mM glucose (G11) +/- 100 nM Ex-4; n = 5. (**F**) Ex-4-induced insulin secretion (fold over G11) in mouse islets from (E). (**G**) Average filipin staining in mouse islets preincubated with Veh or lipoprotein-deficient serum (LPDS) media supplemented with 10 μM simvastatin (LPDS/simv) overnight; n = 5 islet preps from separate mice; representative islet images also shown; size bars, 10 μm. (**H**) Percentage of insulin secretion from mouse islets preincubated with Veh or LPDS/simv before stimulation with G11 +/- 100 nM Ex-4; n = 5. (**I**) Ex-4-induced insulin secretion (fold over G11) in mouse islets from (H). Data is mean +/- SEM; ns, non-significant, *p<0.05, **p<0.01 by paired t-test or one-way ANOVA with Sidak's multiple comparison test.

Figure 2: cgMD simulations of GLP-1R – cholesterol binding sites in model membranes. (**A**) Overview of the simulation setup - GLP-1R is embedded in a model mammalian plasma membrane with the following composition: POPC (30%), DOPC (30%), POPE (8%), DOPE (7%), and cholesterol (25%) in the upper leaflet, and POPC (5%), DOPC (5%), POPE (20%), DOPE (20%), POPS (8%), DOPS (7%), PIP_2 (10%), and cholesterol (10%) in the lower leaflet. (**B**) Average cholesterol occupancy profile in active (left) and inactive (right) GLP-1R states shown as a heatmap (red – highest occupancy; blue – lowest occupancy), with the top 10 highest occupancy residues per state labelled. (**C**) Snake plot showing the top 30 highest cholesterol occupancy residues in active and inactive states, with colours indicating occupancy levels (top 10 – red; top 20 – pink; top 30 – orange). (**D**) Top three cholesterol binding sites in GLP-1R active (top) *versus* inactive (bottom) states, calculated using PyLipID. Binding sites are colour-coded as follows: site I - purple in active and cyan in inactive state; site II - orange; site III - green, with the top 3 residues with the highest residence time in each site labelled and average residence time indicated for each site. (**E**) GLP-1R snake plot indicating residues from top three cholesterol binding sites in both states using the same colour scheme as in (D). (**F**) GLP-1R snake plot indicating the 12 residues selected for screening, with the 4 residues showing a significant reduction in GLP-1R internalisation when mutated to alanine (see H) coloured in red, and the remaining residues in green. (**G**) Table showing the predicted structural impact of the 12 selected residues after site-directed

mutagenesis to alanine in active *vs* inactive GLP-1R using Missense3D-TM (93). (**H**) Surface expression and exendin-4 (100 nM, 10 min) mediated internalisation screen of the 12 selected residues from GLP-1R-cholesterol binding sites mutated to alanine, transiently transfected in INS-1 832/3 GLP-1R KO cells; n = 4-5. Data is mean +/- SEM, *p<0.05, **p<0.01 by one way ANOVA with Dunnett's multiple comparison test *vs* corresponding WT SNAP/FLAG-hGLP-1R.

Figure 3: GLP-1R WT *vs* V229A cholesterol binding propensity. (**A**) Representative images of INS-1 832/3 SNAP/FLAG-hGLP-1R WT or V229A sublines labelled with SNAP-Surface Alexa Fluor 647; size bars, 100 µm. (**B**) Surface expression of SNAP/FLAG-hGLP-1R WT *vs* V229A; n = 6. (**C**) Schematic diagram of the GLP-1R PhotoClick cholesterol binding assay. (**D**) SNAP/FLAG-hGLP-1R-bound cholesterol normalised to receptor levels in INS-1 832/3 SNAP/FLAG-hGLP-1R WT or V229A treated with vehicle (Veh) or 100 nM exendin-4 (Ex-4) for 2 min; n = 4. (**E**) Representative images of INS-1 832/3 SNAP/FLAG-hGLP-1R WT *vs* V229A cells labelled with SNAP-Surface 488 (green) and stimulated with Veh *vs* Ex-4 for 2 min prior to fixation and labelling with D4H*-mCherry (red); size bars, 5 µm. (**F**) Quantification of co-localisation (Mander's tM1) between SNAP/FLAG-hGLP-1R WT or V229A and D4H*-mCherry in cells from (E); n = 5. (**G**) Ex-4 over Veh co-localisation fold change for WT *vs* V229A SNAP/FLAG-hGLP-1R; n = 5. Data is mean +/- SEM, ns, non-significant, *p<0.05, **p<0.01 by paired t-test or one-way ANOVA with Sidak's multiple comparison test.

Figure 4: GLP-1R WT *vs* V229A movement at the plasma membrane. (**A**) Representative images from GLP-1R WT *vs* V229A RICS analysis of plasma membrane lateral diffusion in INS-1 832/3 SNAP/FLAG-hGLP-1R WT or V229A cells labelled with SNAP-Surface Alexa Fluor 647 before stimulation with vehicle (Veh) or 100 nM exendin-4 (Ex-4). (**B**) Average RICS diffusion coefficients from GLP-1R WT *vs* V229A from (A); n = 4. (**C**) TIRF-SPT analysis of average total displacement (top) and speed (bottom) of GLP-1R WT *vs* V229A under Veh or Ex-4-stimulated conditions in INS-1 832/3 GLP-1R KO cells expressing hGLP-1R-mEGFP WT *vs* V229A; n = 4 for total displacement and n = 5 for speed. (**D**) Average RICS diffusion coefficients of the lipid dye Laurdan in INS-1 832/3 SNAP/FLAG-hGLP-1R WT *vs* V229A cells under Veh or Ex-4-stimulated conditions; n = 5. (**E**) Average diffusion coefficient from RICCS analysis of SNAP-Surface Alexa Fluor 647-labelled SNAP/FLAG-hGLP-1R WT *vs* V229A together with lipid-labelled Laurdan under Veh or Ex-4-stimulated conditions in INS-1 832/3 SNAP/FLAG-hGLP-1R WT *vs* V229A cells; n = 5. Data is mean +/- SEM; ns, non-significant, **p<0.05, ***p<0.001 by one-way ANOVA with Sidak's multiple comparison test.

Figure 5: GLP-1R WT *vs* V229A oligomerisation and CCP recruitment. (**A**) N&B estimation of average number of pixels for the different oligomerisation states of the GLP-1R, either as monomers-dimers, dimers-hexamers, hexamers-decamers, or higher order oligomers, calculated at different time frames after stimulation with either vehicle (Veh) or 100 nM exendin-4 (Ex-4) from INS-1 832/3 SNAP/FLAG-hGLP-1R WT or V229A cells; n = 4. (**B**) GLP-1R WT *vs* V229A levels at lipid raft fractions purified from INS-1 832/3 SNAP/FLAG-hGLP-1R WT *vs* V229A cells under Veh or Ex-4-stimulated conditions. Results represent SNAP levels assessed by Western blotting normalised to flotillin as a marker of lipid raft enrichment; n = 5-6. (**C**) Left: representative TIRF images of INS-1 832/3 SNAP/FLAG-hGLP-1R WT or V229A cells co-expressing clathrin light chain-GFP (CLC-GFP) labelled with SNAP-Surface Alexa Fluor 647 prior to Veh or 100 nM Ex-4 stimulation; right: quantification of association ($\Delta F/S$, see Methods) of SNAP/FLAG-hGLP1-R WT or V229A with clathrin puncta; n = 29 and 127 cells for WT Veh *vs* Ex-4, and n = 31 and 106 cells for V229A Veh *vs* Ex-4, respectively; each data point represents mean of 3 cells, data collated from 3 separate experiments. Data is

mean +/- SEM; ns, non-significant, *p<0.05, **p<0.01, ****p<0.0001 by unpaired t-test, one- or two-way ANOVA with Sidak's multiple comparison test.

Figure 6: GLP-1R WT *vs* V229A trafficking profiles. (**A**) Representative images of INS-1 832/3 SNAP/FLAG-hGLP-1R WT or V229A cells labelled with SNAP-Surface Alexa Fluor 647 probe under vehicle (Veh) conditions or following stimulation with 100 nM exendin-4 (Ex-4) for 10 min; size bars, 5 µm. (**B**) Schematic diagram of agonist-mediated SNAP/FLAG-hGLP-1R internalisation assay. (**C**) Percentage of internalised SNAP/FLAG-hGLP-1R WT *vs* V229A at the indicated time points after stimulation with 100 nM Ex-4; corresponding AUC also shown; n = 4. (**D**) Schematic diagram of SNAP/FLAG-hGLP-1R plasma membrane recycling assay. (**E**) Percentage of recycled SNAP/FLAG-hGLP-1R WT *vs* V229A at the indicated time points after stimulation with 100 nM Ex-4; corresponding AUC also shown; n = 3. (**F**) Schematic diagram of agonist-mediated SNAP/FLAG-hGLP-1R degradation assay. (**G**) Percentage of SNAP/FLAG-hGLP-1R WT *vs* V229A degradation at the indicated time points after stimulation with 100 nM Ex-4; corresponding AUC also shown; n = 4. Data is mean +/- SEM; ns, non-significant, *p<0.05, **p<0.01, ***p<0.001 by paired t-test or two-way ANOVA with Sidak's multiple comparison test.

Figure 7: Signalling profiles of GLP-1R WT *vs* V229A. (**A**) Mini-G_s recruitment dose response curves and $\log_{10}(Emax/EC_{50})$ after stimulation with the indicated concentrations of exendin-4 (Ex-4) in INS-1 832/3 GLP-1R KO cells transiently transfected with GLP-1R-SmBiT WT or V229A and LgBiT-mini-G_s; n = 5. (**B**) Mini-G_q recruitment dose response curves and $\log_{10}(Emax/EC_{50})$ after stimulation with the indicated concentrations of Ex-4 in INS-1 832/3 GLP-1R KO cells transiently transfected with GLP-1R-SmBiT WT or V229A and LgBiT-mini-G_q; n = 6. (**C**) β-arrestin 2 (βarr2) recruitment dose response curves and $\log_{10}(Emax/EC_{50})$ after stimulation with the indicated concentrations of Ex-4 in INS-1 832/3 GLP-1R KO cells transiently transfected with GLP-1R-SmBiT WT or V229A and LgBiT-βarr2; n = 5. (**D**) Mini-G_s over βarr2 bias calculation for GLP-1R V229A *vs* WT. (**E**) GLP-1R WT *vs* V229A plasma membrane activation after stimulation with 100 nM Ex-4 in INS-1 832/3 GLP-1R KO cells co-transfected with Nb37-SmBiT, LgBiT-CAAX and SNAP/FLAG-hGLP-1R WT or V229A, measured by NanoBiT bystander complementation assay; AUC also shown; n = 6. (**F**) As in (E) but for GLP-1R WT *vs* V229A endosomal activation in INS-1 832/3 GLP-1R KO cells co-transfected with Nb37-SmBiT, Endofin-LgBiT and SNAP/FLAG-hGLP-1R WT or V229A; n = 6. Data is mean +/- SEM; ns, non-significant, *p<0.05, **p<0.01 by paired t-test or two-way ANOVA with Sidak's multiple comparison test.

Figure 8: Functional responses of GLP-1R WT *vs* V229A in pancreatic beta cells and primary islets. (**A**) cAMP responses of INS-1 832/3 SNAP/FLAG-hGLP-1R WT *vs* V229A cells transduced with the Green Up Global cAMP cADDis biosensor before stimulation with 100 nM Exendin-4 (Ex-4) followed by 100 µM isobutyl methylxanthine (IBMX) + 10 µM forskolin (FSK) for maximal response. (**B**) AUC and maximal response for the Ex-4 period from (A); n = 5. (**C**) Insulin secretion from INS-1 832/3 SNAP/FLAG-hGLP-1R WT *vs* V229A cells following stimulation with 11 mM glucose (G11) +/- 100 nM Ex-4; n = 5. (**D**) Insulin secretion Ex-4-fold increase over G11 calculated from data in (C); n = 5. (**E**) Representative images of GLP-1R KO mouse islets transduced with adenoviruses expressing SNAP/FLAG-hGLP-1R WT or V229A, labelled with SNAP-Surface Alexa Fluor 647 prior to stimulation with vehicle (Veh) or 100 nM Ex-4 for 5 min; size bars, 100 µm. (**F**) Surface expression of SNAP/FLAG-hGLP-1R WT *vs* V229A expressed in GLP-1R KO mouse islets from (E); n = 3. (**G**) Percentage of SNAP/FLAG-hGLP-1R WT *vs* V229A internalisation in GLP-1R KO mouse

islets following stimulation with 100 nM Ex-4 for 5 min; n = 3. (**H**) Insulin secretion responses from GLP-1R KO islets transduced with SNAP/FLAG-hGLP-1R WT *vs* V229A adenoviruses following stimulation with G11 +/- 100 nM Ex-4; n = 3. (**I**) Insulin secretion Ex-4-fold increase over G11 calculated from data in (H); n = 3. Data is mean +/- SEM; ns, non-significant, *p<0.05, **p<0.01 by paired t-test or one-way ANOVA with Sidak's multiple comparison test.

Figure 9: Schematic diagram of effects of cholesterol binding mutant GLP-1R V229A on GLP-1R function. Thick arrows indicate increased and thin arrows decreased pathway engagement.

Supplementary Figure Legends

Supplementary Figure 1: Effect of changes in cholesterol on GLP-1R agonist responses in primary islets - contd. (**A**) cAMP responses in islets isolated from chow *vs* high cholesterol (high chol) diet fed mice transduced with Green Up cADDis biosensor and stimulated with 100 nM exendin-4 (Ex-4) in 6 mM glucose (G6) media followed by 100 µM isobutyl methylxanthine (IBMX) + 10 µM Forskolin (FSK) for maximal response; AUC for Ex-4 stimulation period shown; n = 4. (**B**) cAMP responses in islets isolated from Pdx1$^{Cre\text{-}ERT}$ CAMPER mice (expressing the cAMP reporter ^{T}EPAC^{VV} in beta cells) (63) preincubated with control (Veh) or lipoprotein-deficient serum (LPDS) media supplemented with 10 µM simvastatin (LPDS/simv) overnight and stimulated with 100 nM Ex-4 in G6 followed by 16 mM glucose (G16) and 100 µM IBMX + 10 µM FSK for maximal response; AUC for Ex-4 stimulation period shown; n = 6. (**C**) Representative images from RICS analysis of GLP-1R plasma membrane lateral diffusion in INS-1 832/3 SNAP/FLAG-hGLP-1R cells preincubated with Veh or LPDS/simv media overnight before labelling with SNAP-Surface Alexa Fluor 647 and stimulation with Veh or 100 nM Ex-4. (**D**) Average RICS diffusion coefficient in cells from (C) (n = 5). Data is mean +/- SEM; *p<0.05 by paired t-test or one-way ANOVA with Sidak's multiple comparison test.

Supplementary Figure 2: GLP-1R WT *vs* V229A cholesterol binding, conformational shift and lipid cross-correlation - contd. (**A**) Representative images of bound PhotoClick cholesterol and corresponding SNAP Western blot from SNAP/FLAG-hGLP-1R WT or V229A immunoprecipitation samples; vehicle (Veh), exendin-4 (Ex-4). (**B**) Schematic diagram of GLP-1R conformational shift assay. (**C**) Average conformational shift in response to 100 nM Ex-4 stimulation in INS-1 832/3 SNAP/FLAG-hGLP-1R WT *vs* V229A; AUC of conformational shift response shown; n = 6. (**D**) Representative images from GLP-1R WT *vs* V229A RICCS analysis of plasma membrane lateral diffusion in INS-1 832/3 SNAP/FLAG-hGLP-1R WT or V229A cells labelled with SNAP-Surface Alexa Fluor 647 (red) and Laurdan (blue) before stimulation with Veh or 100 nM Ex-4. Data is mean +/- SEM; ns, not significant using paired t-test.

References

1. Graaf Cd, Donnelly D, Wootten D, Lau J, Sexton PM, Miller LJ, et al. Glucagon-Like Peptide-1 and Its Class B G Protein–Coupled Receptors: A Long March to Therapeutic Successes. Pharmacological Reviews. 2016;68(4):954.

2. Boer GA, Holst JJ. Incretin hormones and type 2 diabetes—Mechanistic insights and therapeutic approaches. Biology2020.

3. Gutierrez-Aguilar R, Woods SC. Nutrition and L and K-enteroendocrine cells. Current Opinion in Endocrinology, Diabetes and Obesity. 2011;18(1).

4. Holst JJ. The Physiology of Glucagon-like Peptide 1. Physiological Reviews. 2007;87(4):1409-39.

5. Drucker DJ, Holst JJ. The expanding incretin universe: from basic biology to clinical translation. Diabetologia. 2023;66(10):1765-79.

6. El Eid L, Reynolds CA, Tomas A, Ben J. Biased agonism and polymorphic variation at the GLP-1 receptor: Implications for the development of personalised therapeutics. Pharmacological Research. 2022;184:106411.

7. Miller LJ, Sexton PM, Dong M, Harikumar KG. The class B G-protein-coupled GLP-1 receptor: an important target for the treatment of type-2 diabetes mellitus. Int J Obes Suppl. 2014;4(Suppl 1):S9-S13.

8. Camilleri M, Acosta A. Newer pharmacological interventions directed at gut hormones for obesity. Br J Pharmacol. 2024;181(8):1153-64.

9. Lu W, Zhou Z, Jiang N, Han J. An updated patent review of GLP-1 receptor agonists (2020-present). Expert Opin Ther Pat. 2023;33(9):597-612.

10. Smelcerovic A, Lazarevic J, Tomovic K, Anastasijevic M, Jukic M, Kocic G, et al. An Overview, Advantages and Therapeutic Potential of Nonpeptide Positive Allosteric Modulators of Glucagon-Like Peptide-1 Receptor. ChemMedChem. 2019;14(5):514-21.

11. Cong Z, Chen LN, Ma H, Zhou Q, Zou X, Ye C, et al. Molecular insights into ago-allosteric modulation of the human glucagon-like peptide-1 receptor. Nat Commun. 2021;12(1):3763.

12. Müller TD, Finan B, Clemmensen C, DiMarchi RD, Tschöp MH. The New Biology and Pharmacology of Glucagon. Physiological Reviews. 2017;97(2):721-66.

13. Drucker DJ, Yusta B. Physiology and Pharmacology of the Enteroendocrine Hormone Glucagon-Like Peptide-2. Annual Review of Physiology. 2014;76(1):561-83.

14. Bortolato A, Doré AS, Hollenstein K, Tehan BG, Mason JS, Marshall FH. Structure of Class B GPCRs: New horizons for drug discovery. British Journal of Pharmacology2014.

15. Baccouch R, Rascol E, Stoklosa K, Alves ID. The role of the lipid environment in the activity of G protein coupled receptors. Biophysical Chemistry. 2022;285:106794.

16. Marzook A, Tomas A, Jones B. The Interplay of Glucagon-Like Peptide-1 Receptor Trafficking and Signalling in Pancreatic Beta Cells. Frontiers in endocrinology. 2021;12:678055-.

17. Sezgin E, Levental I, Mayor S, Eggeling C. The mystery of membrane organization: composition, regulation and roles of lipid rafts. Nature Reviews Molecular Cell Biology. 2017;18(6):361-74.

18. Bernardino de la Serna J, Schutz GJ, Eggeling C, Cebecauer M. There Is No Simple Model of the Plasma Membrane Organization. Front Cell Dev Biol. 2016;4:106.

19. Kumar GA, Chattopadhyay A. Cholesterol-dependent endocytosis of GPCRs: implications in pathophysiology and therapeutics. Biophys Rev. 2021;13(6):1007-17.

20. Sunshine H, Iruela-Arispe ML. Membrane lipids and cell signaling. Curr Opin Lipidol. 2017;28(5):408-13.

21. McGraw C, Koretz KS, Oseid D, Lyman E, Robinson AS. Cholesterol Dependent Activity of the Adenosine A2A Receptor Is Modulated via the Cholesterol Consensus Motif. Molecules. 2022;27(11):3529.

22. Hanson MA, Cherezov V, Griffith MT, Roth CB, Jaakola V-P, Chien EYT, et al. A Specific Cholesterol Binding Site Is Established by the 2.8 Å Structure of the Human β2-Adrenergic Receptor. Structure. 2008;16(6):897-905.

23. Sejdiu BI, Tieleman DP. Lipid-Protein Interactions Are a Unique Property and Defining Feature of G Protein-Coupled Receptors. Biophysical Journal. 2020;118(8):1887-900.

24. Shrivastava S, Sarkar P, Preira P, Salomé L, Chattopadhyay A. Cholesterol-Dependent Dynamics of the Serotonin1A Receptor Utilizing Single Particle Tracking: Analysis of Diffusion Modes. The Journal of Physical Chemistry B. 2022;126(35):6682-90.

25. Buenaventura T, Bitsi S, Laughlin WE, Burgoyne T, Lyu Z, Oqua AI, et al. Agonist-induced membrane nanodomain clustering drives GLP-1 receptor responses in pancreatic beta cells. PLoS Biology. 2019;17(8).

26. Pedersen TR, Tobert JA. Simvastatin: a review. Expert Opin Pharmacother. 2004;5(12):2583-96.

27. Naylor J, Suckow AT, Seth A, Baker DJ, Sermadiras I, Ravn P, et al. Use of CRISPR/Cas9-engineered INS-1 pancreatic beta cells to define the pharmacology of dual GIPR/GLP-1R agonists. Biochem J. 2016;473(18):2881-91.

28. Manchanda Y, Bitsi S, Chen S, Broichhagen J, Bernardino de la Serna J, Jones B, et al. Enhanced Endosomal Signaling and Desensitization of GLP-1R vs GIPR in Pancreatic Beta Cells. Endocrinology. 2023;164(5).

29. Song W, Corey RA, Ansell TB, Cassidy CK, Horrell MR, Duncan AL, et al. PyLipID: A Python Package for Analysis of Protein–Lipid Interactions from Molecular Dynamics Simulations. Journal of Chemical Theory and Computation. 2022;18(2):1188-201.

30. Zhang Y, Sun B, Feng D, Hu H, Chu M, Qu Q, et al. Cryo-EM structure of the activated GLP-1 receptor in complex with a G protein. Nature. 2017;546(7657):248-53.

31. Buenaventura T, Bitsi S, Laughlin WE, Burgoyne T, Lyu Z, Oqua AI, et al. Agonist-induced membrane nanodomain clustering drives GLP-1 receptor responses in pancreatic beta cells. PLoS Biol. 2019;17(8):e3000097.

32. Lim CY, Davis OB, Shin HR, Zhang J, Berdan CA, Jiang X, et al. ER-lysosome contacts enable cholesterol sensing by mTORC1 and drive aberrant growth signalling in Niemann-Pick type C. Nat Cell Biol. 2019;21(10):1206-18.

33. Pickford P, Lucey M, Fang Z, Bitsi S, de la Serna JB, Broichhagen J, et al. Signalling, trafficking and glucoregulatory properties of glucagon-like peptide-1 receptor agonists exendin-4 and lixisenatide. Br J Pharmacol. 2020;177(17):3905-23.

34. Brewer J, Bernardino de la Serna J, Wagner K, Bagatolli LA. Multiphoton excitation fluorescence microscopy in planar membrane systems. Biochim Biophys Acta. 2010;1798(7):1301-8.

35. Lorizate M, Terrones O, Nieto-Garai JA, Rojo-Bartolome I, Ciceri D, Morana O, et al. Super-Resolution Microscopy Using a Bioorthogonal-Based Cholesterol Probe Provides Unprecedented Capabilities for Imaging Nanoscale Lipid Heterogeneity in Living Cells. Small Methods. 2021;5(9):e2100430.

36. Asalla S, Girada SB, Kuna RS, Chowdhury D, Kandagatla B, Oruganti S, et al. Restoring Mitochondrial Function: A Small Molecule-mediated Approach to Enhance Glucose Stimulated Insulin Secretion in Cholesterol Accumulated Pancreatic beta cells. Scientific Reports. 2016;6(1):27513.

37. Akter R, Hogan MF, Esser N, Castillo JJ, Hull-Meichle RL, Zraika S, et al. 1457-P: Cholesterol Accumulation in Islets Increases Steroidogenic Acute Regulatory (StAR) Protein Expression and Decreases Islet Cell Viability and ß-Cell Function. Diabetes. 2022;71(Supplement_1).

38. Manna PR, Stetson CL, Slominski AT, Pruitt K. Role of the steroidogenic acute regulatory protein in health and disease. Endocrine. 2016;51(1):7-21.

39. Hogan MF, Ziemann M, K N H, Rodriguez H, Kaspi A, Esser N, et al. RNA-seq-based identification of Star upregulation by islet amyloid formation. Protein Engineering, Design and Selection. 2019;32(2):67-76.

40. Hogan MF, Esser N, Templin AT, Zraika S, Hull RL, El-Osta S, et al. 2125-P: Increased StAR (Steroidogenic Acute Regulatory Protein) Is Detrimental to β Cells and Promotes Mitochondrial Dysfunction. Diabetes. 2019;68(Supplement_1).

41. Austin G, ElEid L, Oqua AI, Manchanda M, Poliakova Y, Bouzakri K, Montoya A, Withers DJ, Jones B, Millership SJ, Prokopenko I, Tomas A. An inter-organelle contact between endosomal GLP-1R, ER VAP-B, and the mitochondrial AKAP SPHKAP triggers PKA-dependent MIC19 phosphorylation and β-cell mitochondrial remodelling. bioRxiv2024.

42. Kang MY, Oh TJ, Cho YM. Glucagon-Like Peptide-1 Increases Mitochondrial Biogenesis and Function in INS-1 Rat Insulinoma Cells. Endocrinol Metab (Seoul). 2015;30(2):216-20.

43. Ježek P, Holendová B, Jabůrek M, Dlasková A, Plecitá-Hlavatá L. Contribution of Mitochondria to Insulin Secretion by Various Secretagogues. Antioxidants & Redox Signaling. 2022;36(13-15):920-52.

44. Röhrl C, Stangl H. Cholesterol metabolism-physiological regulation and pathophysiological deregulation by the endoplasmic reticulum. Wien Med Wochenschr. 2018;168(11-12):280-5.

45. Friesen JA, Rodwell VW. The 3-hydroxy-3-methylglutaryl coenzyme-A (HMG-CoA) reductases. Genome Biol. 2004;5(11):248.

46. Plosker GL, McTavish D. Simvastatin. Drugs. 1995;50(2):334-63.

47. Mahammad S, Parmryd I. Cholesterol homeostasis in T cells. Methyl-β-cyclodextrin treatment results in equal loss of cholesterol from Triton X-100 soluble and insoluble fractions. Biochimica et Biophysica Acta (BBA) - Biomembranes. 2008;1778(5):1251-8.

48. Yaluri N, Modi S, López Rodríguez M, Stančáková A, Kuusisto J, Kokkola T, et al. Simvastatin Impairs Insulin Secretion by Multiple Mechanisms in MIN6 Cells. PLOS ONE. 2015;10(11):e0142902.

49. Laakso M, Fernandes Silva L. Statins and risk of type 2 diabetes: mechanism and clinical implications. Front Endocrinol (Lausanne). 2023;14:1239335.

50. Buldak L, Machnik G, Skudrzyk E, Boldys A, Maliglowka M, Kosowski M, et al. Exenatide prevents statin-related LDL receptor increase and improves insulin secretion in pancreatic beta cells (1.1E7) in a protein kinase A-dependent manner. J Appl Biomed. 2022;20(4):130-40.

51. Corradi V, Mendez-Villuendas E, Ingólfsson HI, Gu R-X, Siuda I, Melo MN, et al. Lipid–Protein Interactions Are Unique Fingerprints for Membrane Proteins. ACS Central Science. 2018;4(6):709-17.

52. Jafurulla M, Tiwari S, Chattopadhyay A. Identification of cholesterol recognition amino acid consensus (CRAC) motif in G-protein coupled receptors. Biochemical and Biophysical Research Communications. 2011;404(1):569-73.

53. Zhang X, Belousoff MJ, Zhao P, Kooistra AJ, Truong TT, Ang SY, et al. Differential GLP-1R Binding and Activation by Peptide and Non-peptide Agonists. Molecular Cell. 2020;80(3):485-500.e7.

54. Taghon GJ, Rowe JB, Kapolka NJ, Isom DG. Predictable cholesterol binding sites in GPCRs lack consensus motifs. Structure. 2021;29(5):499-506.e3.

55. Wu F, Yang L, Hang K, Laursen M, Wu L, Han GW, et al. Full-length human GLP-1 receptor structure without orthosteric ligands. Nature Communications. 2020;11(1):1272.

56. Liang Y-L, Khoshouei M, Glukhova A, Furness SGB, Zhao P, Clydesdale L, et al. Phase-plate cryo-EM structure of a biased agonist-bound human GLP-1 receptor–Gs complex. Nature. 2018;555(7694):121-5.

57. Rossow MJ, Sasaki JM, Digman MA, Gratton E. Raster image correlation spectroscopy in live cells. Nature Protocols. 2010;5(11):1761-74.

58. Gunther G, Malacrida L, Jameson DM, Gratton E, Sánchez SA. LAURDAN since Weber: The Quest for Visualizing Membrane Heterogeneity. Accounts of Chemical Research. 2021;54(4):976-87.

59. Jones B. The therapeutic potential of GLP-1 receptor biased agonism. Br J Pharmacol. 2022;179(4):492-510.

60. Jones B, Buenaventura T, Kanda N, Chabosseau P, Owen BM, Scott R, et al. Targeting GLP-1 receptor trafficking to improve agonist efficacy. Nature Communications. 2018;9(1).

61. Moreau CJ, Audic G, Lemel L, García-Fernández MD, Nieścierowicz K. Interactions of cholesterol molecules with GPCRs in different states: A comparative analysis of GPCRs' structures. Biochimica et Biophysica Acta (BBA) - Biomembranes. 2023;1865(3):184100.

62. Jakubík J, El-Fakahany EE. Allosteric Modulation of GPCRs of Class A by Cholesterol. International Journal of Molecular Sciences. 2021;22(4):1953.

63. Bitsi S, El Eid L, Manchanda Y, Oqua AI, Mohamed N, Hansen B, et al. Divergent acute versus prolonged pharmacological GLP-1R responses in adult beta cell-specific beta-arrestin 2 knockout mice. Sci Adv. 2023;9(18):eadf7737.

64. Hohmeier HE, Mulder H, Chen G, Henkel-Rieger R, Prentki M, Newgard CB. Isolation of INS-1-derived cell lines with robust ATP-sensitive K+ channel-dependent and -independent glucose-stimulated insulin secretion. Diabetes. 2000;49(3):424-30.

65. Pándy-Szekeres G, Caroli J, Mamyrbekov A, Kermani AA, Keserű GM, Kooistra AJ, et al. GPCRdb in 2023: state-specific structure models using AlphaFold2 and new ligand resources. Nucleic Acids Res. 2023;51(D1):D395-d402.

66. Zhang X, Johnson RM, Drulyte I, Yu L, Kotecha A, Danev R, et al. Evolving cryo-EM structural approaches for GPCR drug discovery. Structure. 2021;29(9):963-74.e6.

67. Eswar N, Webb B, Marti-Renom MA, Madhusudhan MS, Eramian D, Shen MY, et al. Comparative protein structure modeling using Modeller. Curr Protoc Bioinformatics. 2006;Chapter 5:Unit-5.6.

68. P C Kroon FG, J Barnoud, M van Tilburg, P C T Souza, T A Wassenaar, S J Marrink. Martinize2 and Vermouth: Unified Framework for Topology Generation2023.

69. Souza PCT, Alessandri R, Barnoud J, Thallmair S, Faustino I, Grünewald F, et al. Martini 3: a general purpose force field for coarse-grained molecular dynamics. Nature Methods. 2021;18(4):382-8.

70. Periole X, Cavalli M, Marrink S-J, Ceruso MA. Combining an Elastic Network With a Coarse-Grained Molecular Force Field: Structure, Dynamics, and Intermolecular Recognition. Journal of Chemical Theory and Computation. 2009;5(9):2531-43.

71. Lomize AL, Todd SC, Pogozheva ID. Spatial arrangement of proteins in planar and curved membranes by PPM 3.0. Protein Sci. 2022;31(1):209-20.

72. Wassenaar TA, Ingólfsson HI, Böckmann RA, Tieleman DP, Marrink SJ. Computational Lipidomics with insane: A Versatile Tool for Generating Custom Membranes for Molecular Simulations. Journal of Chemical Theory and Computation. 2015;11(5):2144-55.

73. Song W, Yen H-Y, Robinson CV, Sansom MSP. State-dependent Lipid Interactions with the A2a Receptor Revealed by MD Simulations Using In Vivo-Mimetic Membranes. Structure. 2019;27(2):392-403.e3.

74. Borges-Araújo L, Souza PCT, Fernandes F, Melo MN. Improved Parameterization of Phosphatidylinositide Lipid Headgroups for the Martini 3 Coarse-Grain Force Field. Journal of Chemical Theory and Computation. 2022;18(1):357-73.

75. Borges-Araújo L, Borges-Araújo AC, Ozturk TN, Ramirez-Echemendia DP, Fábián B, Carpenter TS, et al. Martini 3 Coarse-Grained Force Field for Cholesterol. Journal of Chemical Theory and Computation. 2023;19(20):7387-404.

76. Qi Y, Ingólfsson HI, Cheng X, Lee J, Marrink SJ, Im W. CHARMM-GUI Martini Maker for Coarse-Grained Simulations with the Martini Force Field. Journal of Chemical Theory and Computation. 2015;11(9):4486-94.

77. Bussi G, Donadio D, Parrinello M. Canonical sampling through velocity rescaling. The Journal of Chemical Physics. 2007;126(1).

78. Parrinello M, Rahman A. Polymorphic transitions in single crystals: A new molecular dynamics method. Journal of Applied Physics. 1981;52(12):7182-90.

79. Abraham MJ, Murtola T, Schulz R, Páll S, Smith JC, Hess B, et al. GROMACS: High performance molecular simulations through multi-level parallelism from laptops to supercomputers. SoftwareX. 2015;1-2:19-25.

80. Humphrey W, Dalke A, Schulten K. VMD: Visual molecular dynamics. Journal of Molecular Graphics. 1996;14(1):33-8.

81. Bernabe-Rubio M, Bosch-Fortea M, Alonso MA, Bernardino de la Serna J. Multi-dimensional and spatiotemporal correlative imaging at the plasma membrane of live cells to determine the continuum nano-to-micro scale lipid adaptation and collective motion. Methods. 2021;193:136-47.

82. Garcia E, Bernardino de la Serna J. Dissecting single-cell molecular spatiotemporal mobility and clustering at focal adhesions in polarised cells by fluorescence fluctuation spectroscopy methods. Methods. 2018;140-141:85-96.

83. Pickford P, Lucey M, Fang Z, Bitsi S, de la Serna JB, Broichhagen J, et al. Signalling, trafficking and glucoregulatory properties of glucagon-like peptide-1 receptor agonists exendin-4 and lixisenatide. British Journal of Pharmacology. 2020;177(17):3905-23.

84. Garcia E, Bernardino de la Serna J. Dissecting single-cell molecular spatiotemporal mobility and clustering at focal adhesions in polarised cells by fluorescence fluctuation spectroscopy methods. Methods. 2018;140-141.

85. Bernabé-Rubio M, Bosch-Fortea M, García E, Bernardino de la Serna J, Alonso MA. Adaptive Lipid Immiscibility and Membrane Remodeling Are Active Functional Determinants of Primary Ciliogenesis. Small Methods. 2021;5(2):2000711.

86. Syme CA, Zhang L, Bisello A. Caveolin-1 regulates cellular trafficking and function of the glucagon-like Peptide 1 receptor. Mol Endocrinol. 2006;20(12):3400-11.

87. Salavessa L, Sauvonnet N. Stoichiometry of ReceptorsReceptors at the Plasma MembranePlasma membrane During Their EndocytosisEndocytosis Using Total Internal Reflection Fluorescent (TIRF) MicroscopyMicroscopy Live Imaging and Single-Molecule Tracking. In: Niedergang F, Vitale N, Gasman S, editors. Exocytosis and Endocytosis: Methods and Protocols. New York, NY: Springer US; 2021. p. 3-17.

88. Klymchenko AS. Fluorescent Probes for Lipid Membranes: From the Cell Surface to Organelles. Acc Chem Res. 2023;56(1):1-12.

89. Lucey M, Ashik T, Marzook A, Wang Y, Goulding J, Oishi A, et al. Acylation of the incretin peptide exendin-4 directly impacts GLP-1 receptor signalling and trafficking. bioRxiv. 2021:2021.04.01.438030.

90. Barg S, Knowles MK, Chen X, Midorikawa M, Almers W. Syntaxin clusters assemble reversibly at sites of secretory granules in live cells. Proceedings of the National Academy of Sciences. 2010;107(48):20804-9.

91. Fang Z, Chen S, Manchanda Y, Bitsi S, Pickford P, David A, et al. Ligand-Specific Factors Influencing GLP-1 Receptor Post-Endocytic Trafficking and Degradation in Pancreatic Beta Cells. International journal of molecular sciences. 2020;21(21):8404.

92. Jones B, McGlone ER, Fang Z, Pickford P, Corrêa IR, Oishi A, et al. Genetic and biased agonist-mediated reductions in β-arrestin recruitment prolong cAMP signaling at glucagon family receptors. Journal of Biological Chemistry. 2021;296:100133.

93. Hanna G, Khanna T, Islam SA, David A, Sternberg MJE. Missense3D-TM: Predicting the Effect of Missense Variants in Helical Transmembrane Protein Regions Using 3D Protein Structures. Journal of Molecular Biology. 2024;436(2):168374.

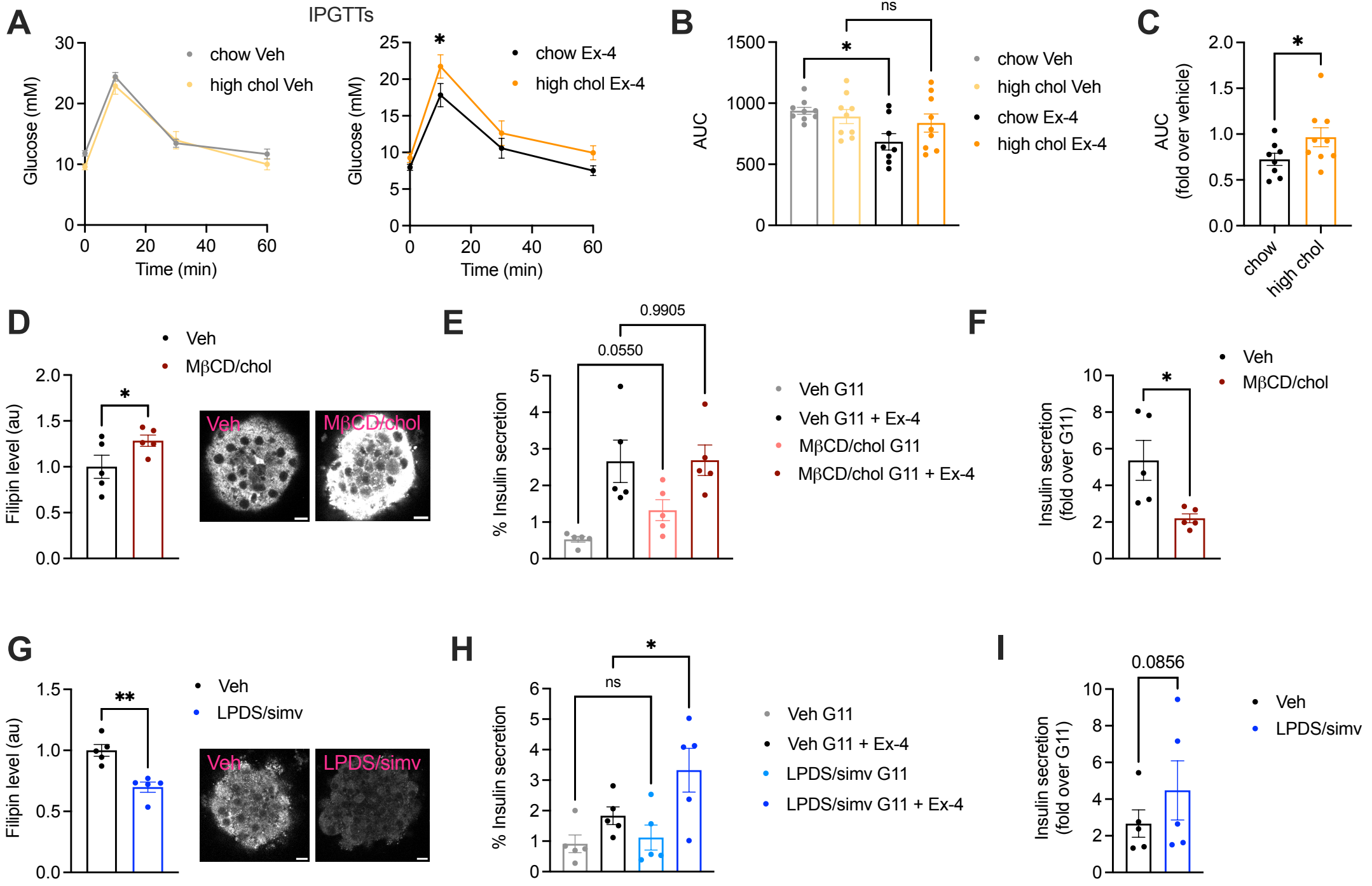
A
IPGTTs
Glucose (mM)
Time (min)
chow Veh
high chol Veh
chow Ex-4
high chol Ex-4
*
B
ns
AUC
C
AUC (fold over vehicle)
chow
high chol
D
Veh
MβCD/chol
Filipin level (au)
E
0.9905
0.0550
% Insulin secretion
Veh G11
Veh G11 + Ex-4
MβCD/chol G11
MβCD/chol G11 + Ex-4
F
Insulin secretion (fold over G11)
G
**
LPDS/simv
H
ns
Veh G11
Veh G11 + Ex-4
LPDS/simv G11
LPDS/simv G11 + Ex-4
I
0.0856

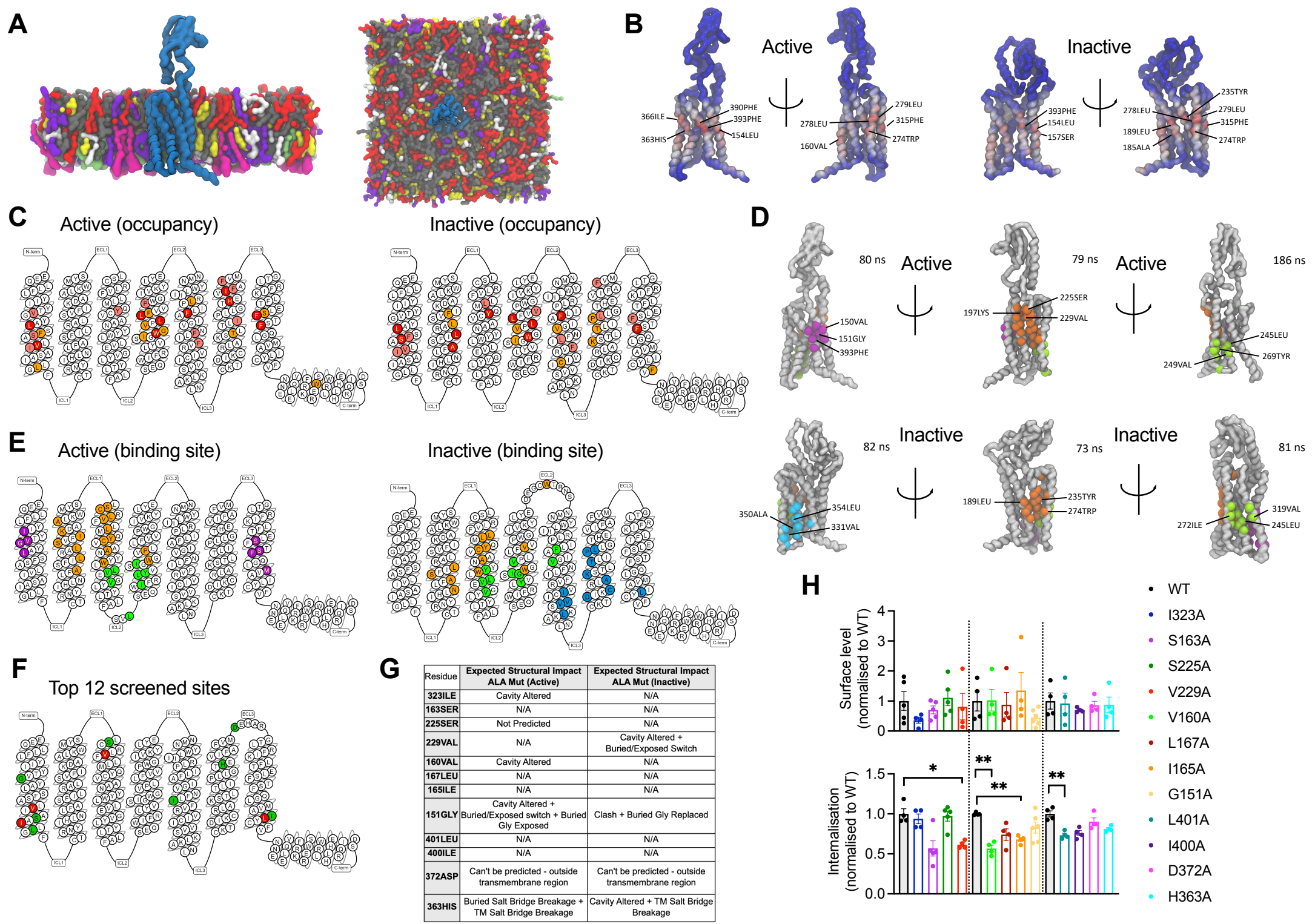

Residue	Expected Structural Impact ALA Mut (Active)	Expected Structural Impact ALA Mut (Inactive)
323ILE	Cavity Altered	N/A
163SER	N/A	N/A
225SER	Not Predicted	N/A
229VAL	N/A	Cavity Altered + Buried/Exposed Switch
160VAL	Cavity Altered	N/A
167LEU	N/A	N/A
165ILE	N/A	N/A
151GLY	Cavity Altered + Buried/Exposed switch + Buried Gly Exposed	Clash + Buried Gly Replaced
401LEU	N/A	N/A
400ILE	N/A	N/A
372ASP	Can't be predicted - outside transmembrane region	Can't be predicted - outside transmembrane region
363HIS	Buried Salt Bridge Breakage + TM Salt Bridge Breakage	Cavity Altered + TM Salt Bridge Breakage

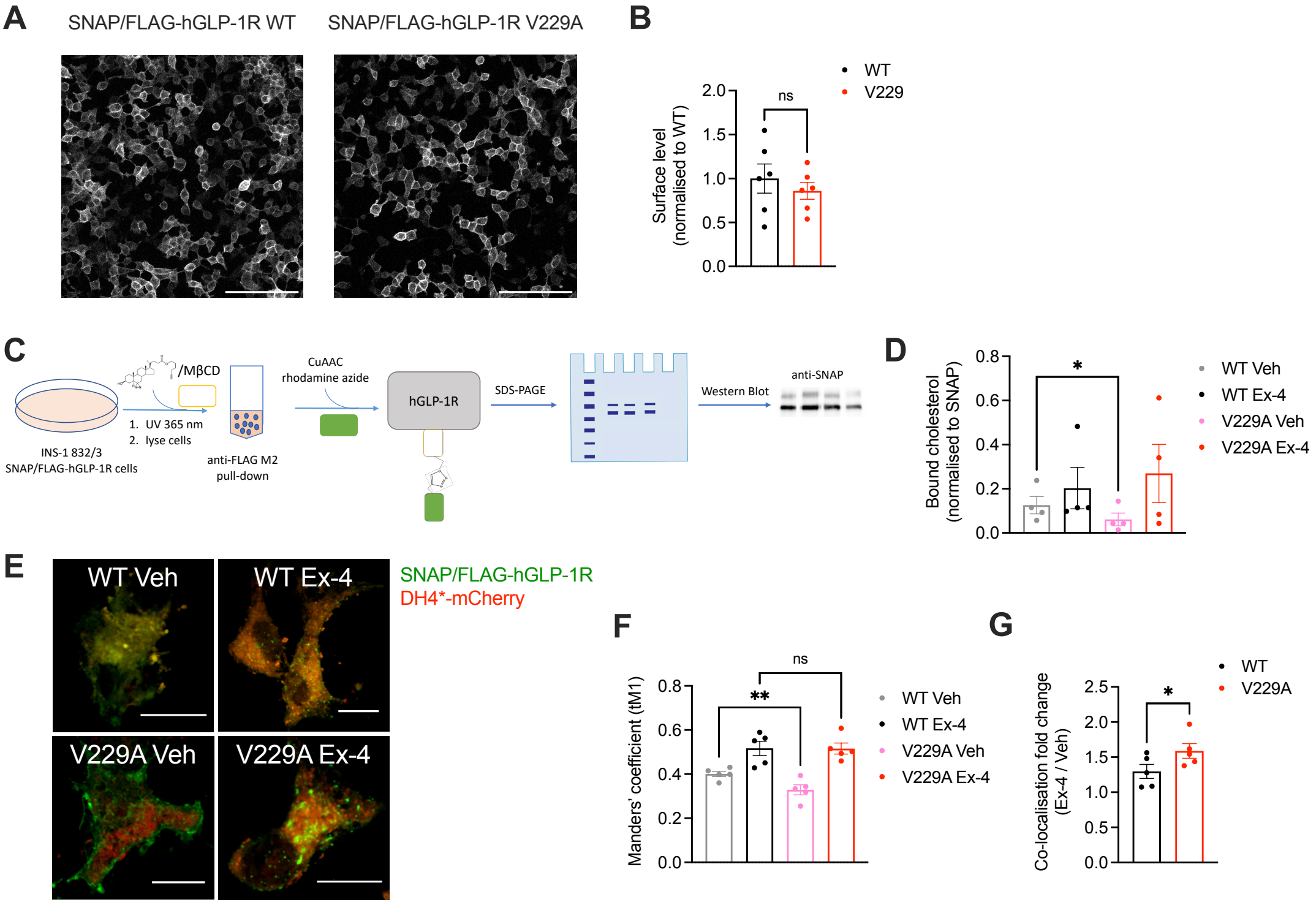
A
SNAP/FLAG-hGLP-1R WT
SNAP/FLAG-hGLP-1R V229A
B
WT
V229
ns
Surface level (normalised to WT)
2.0
1.5
1.0
0.5
0.0
C
/MβCD
1. UV 365 nm
2. lyse cells
INS-1 832/3
SNAP/FLAG-hGLP-1R cells
anti-FLAG M2
pull-down
CuAAC
rhodamine azide
hGLP-1R
SDS-PAGE
Western Blot
anti-SNAP
D
Bound cholesterol (normalised to SNAP)
0.8
0.6
0.4
0.2
0.0
*
WT Veh
WT Ex-4
V229A Veh
V229A Ex-4
E
WT Veh
WT Ex-4
V229A Veh
V229A Ex-4
SNAP/FLAG-hGLP-1R
DH4*-mCherry
F
Manders' coefficient (tM1)
0.8
0.6
0.4
0.2
0.0
ns
**
WT Veh
WT Ex-4
V229A Veh
V229A Ex-4
G
Co-localisation fold change (Ex-4 / Veh)
2.5
2.0
1.5
1.0
0.5
0.0
*
WT
V229A

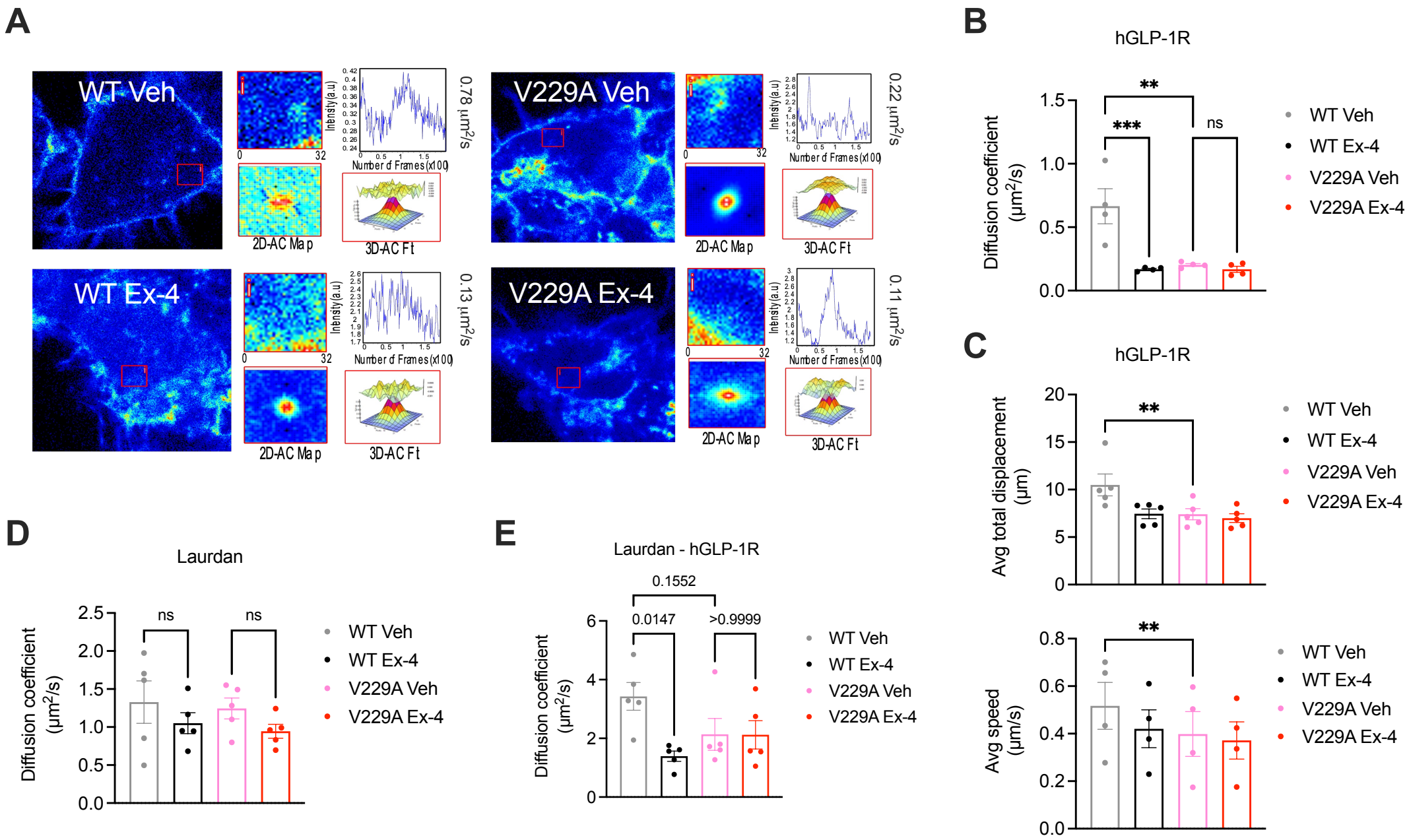
A
WT Veh
0.78 μm²/s
V229A Veh
0.22 μm²/s
WT Ex-4
0.13 μm²/s
V229A Ex-4
0.11 μm²/s
Intensity (a.u)
Number of Frames (x100)
2D-AC Map
3D-AC Ft
B
hGLP-1R
Diffusion coefficient (μm²/s)
**
***
ns
WT Veh
WT Ex-4
V229A Veh
V229A Ex-4
C
hGLP-1R
Avg total displacement (μm)
Avg speed (μm/s)
D
Laurdan
E
Laurdan - hGLP-1R
0.1552
0.0147
>0.9999

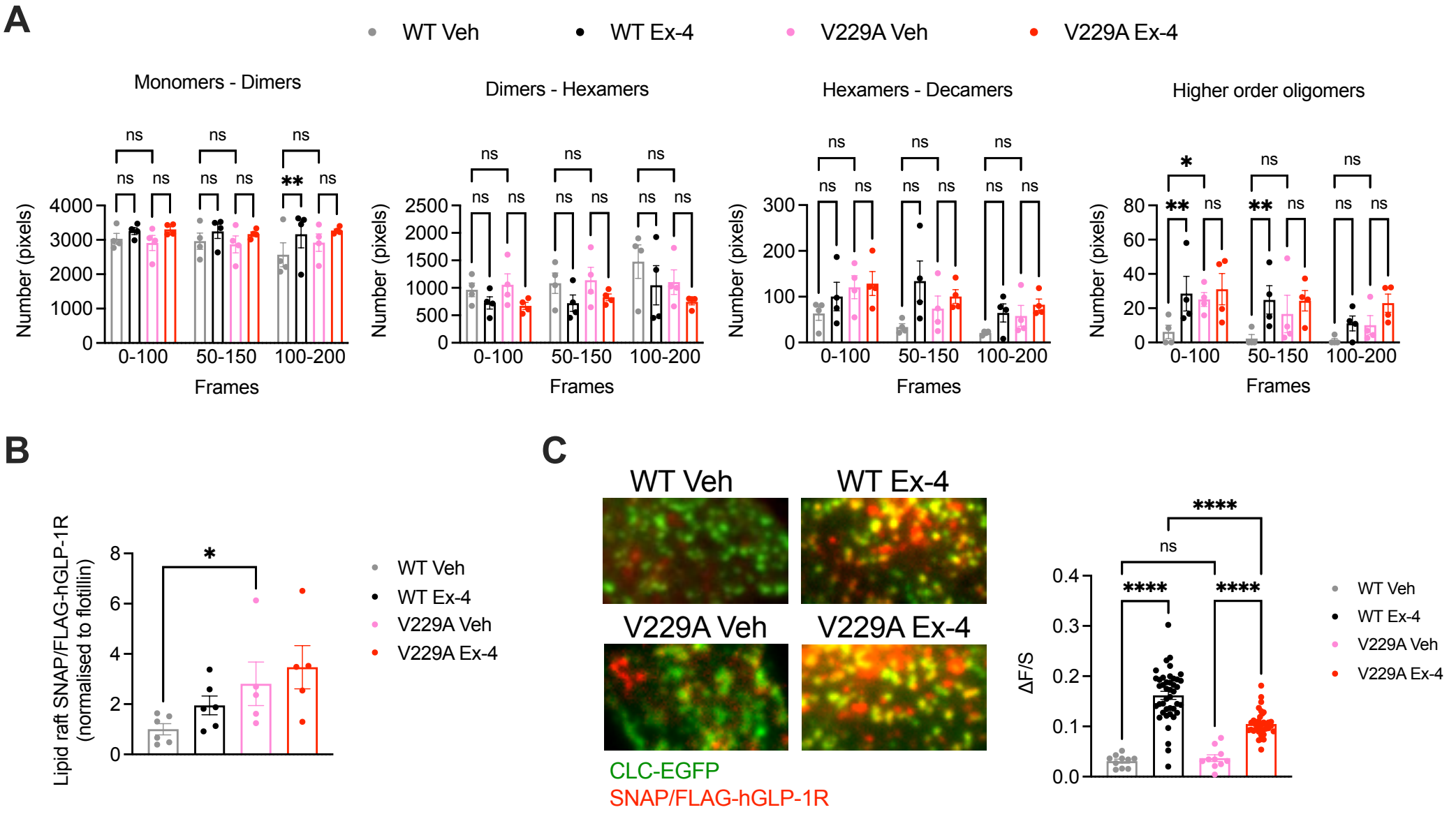
A
WT Veh
WT Ex-4
V229A Veh
V229A Ex-4
Monomers - Dimers
Dimers - Hexamers
Hexamers - Decamers
Higher order oligomers
Number (pixels)
Frames
0-100
50-150
100-200
ns
**
*
B
Lipid raft SNAP/FLAG-hGLP-1R (normalised to flotillin)
C
WT Veh
WT Ex-4
V229A Veh
V229A Ex-4
CLC-EGFP
SNAP/FLAG-hGLP-1R
ΔF/S
****

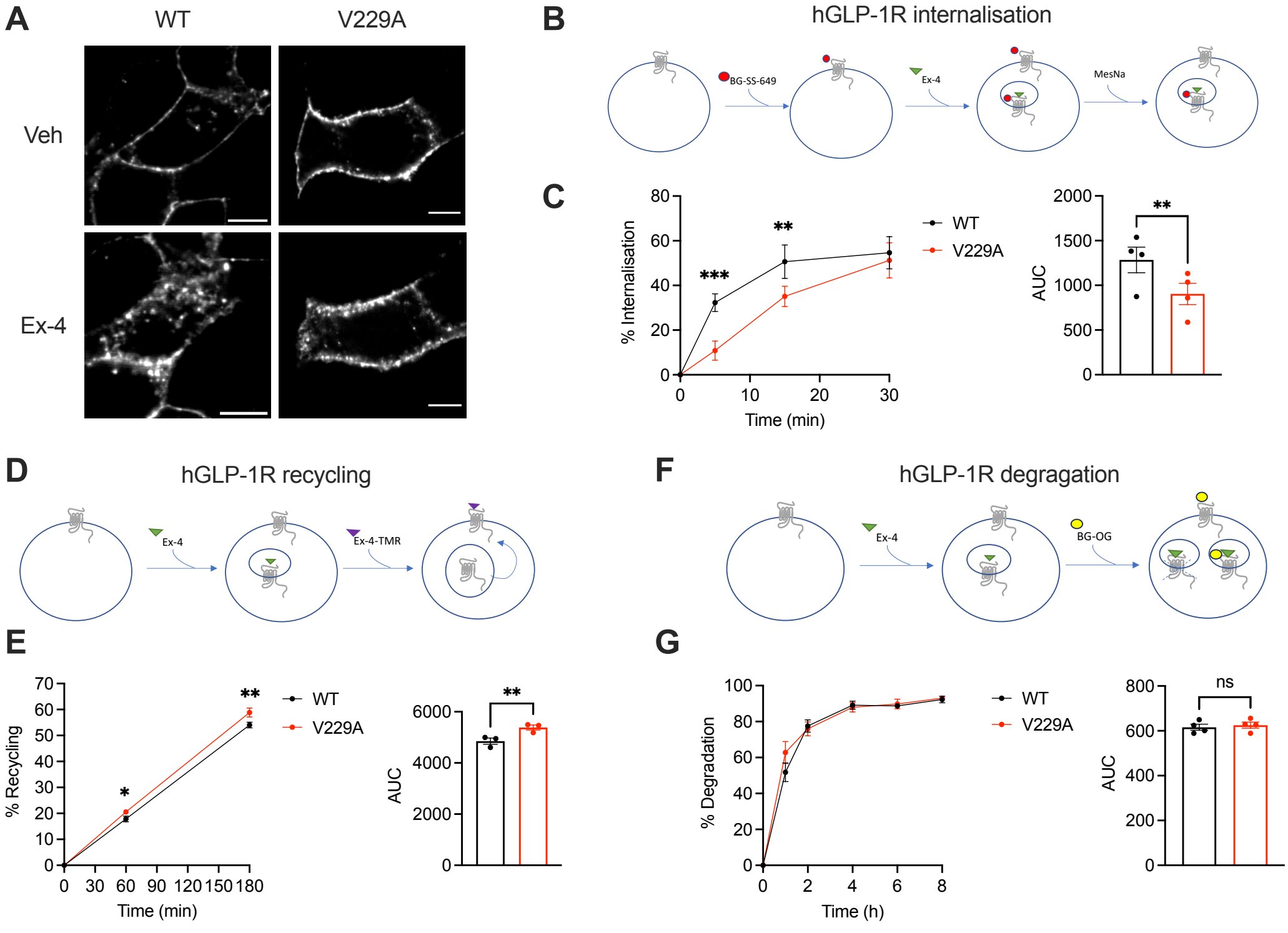
A
WT
V229A
Veh
Ex-4
B
hGLP-1R internalisation
BG-SS-649
Ex-4
MesNa
C
% Internalisation
Time (min)
WT
V229A
***
**
AUC
**
D
hGLP-1R recycling
Ex-4
Ex-4-TMR
E
% Recycling
Time (min)
WT
V229A
*
**
AUC
**
F
hGLP-1R degragation
Ex-4
BG-OG
G
% Degradation
Time (h)
WT
V229A
AUC
ns

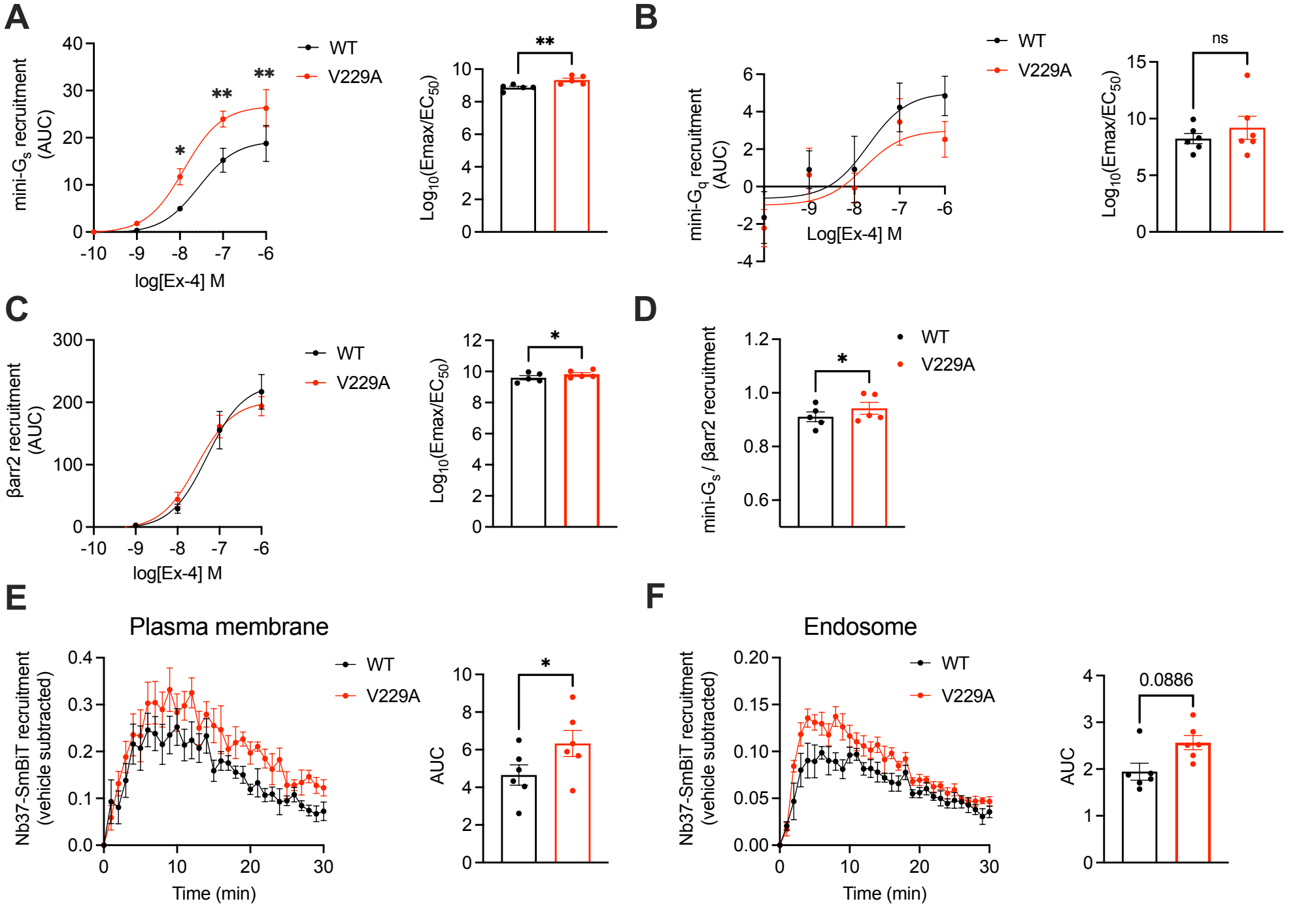
A
mini-Gs recruitment (AUC)
log[Ex-4] M
WT
V229A
Log10(Emax/EC50)
B
mini-Gq recruitment (AUC)
Log[Ex-4] M
ns
C
βarr2 recruitment (AUC)
log[Ex-4] M
D
mini-Gs / βarr2 recruitment
E
Plasma membrane
Nb37-SmBiT recruitment (vehicle subtracted)
Time (min)
AUC
F
Endosome
0.0886

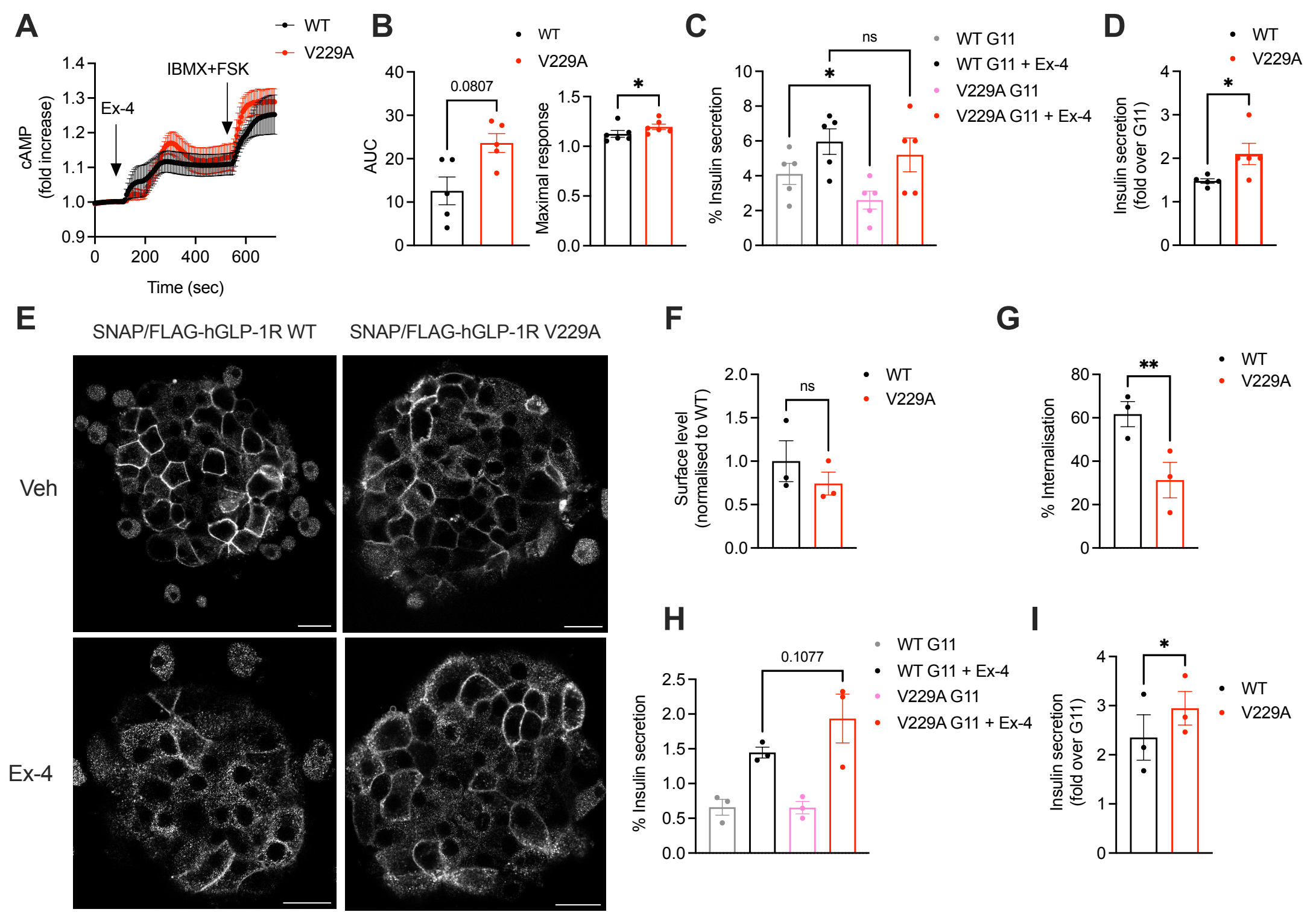
A
WT
V229A
IBMX+FSK
Ex-4
cAMP (fold increase)
Time (sec)
B
WT
V229A
0.0807
AUC
Maximal response
C
ns
WT G11
WT G11 + Ex-4
V229A G11
V229A G11 + Ex-4
% Insulin secretion
D
WT
V229A
Insulin secretion (fold over G11)
E
SNAP/FLAG-hGLP-1R WT
SNAP/FLAG-hGLP-1R V229A
Veh
Ex-4
F
ns
WT
V229A
Surface level (normalised to WT)
G
WT
V229A
% Internalisation
H
0.1077
WT G11
WT G11 + Ex-4
V229A G11
V229A G11 + Ex-4
% Insulin secretion
I
WT
V229A
Insulin secretion (fold over G11)

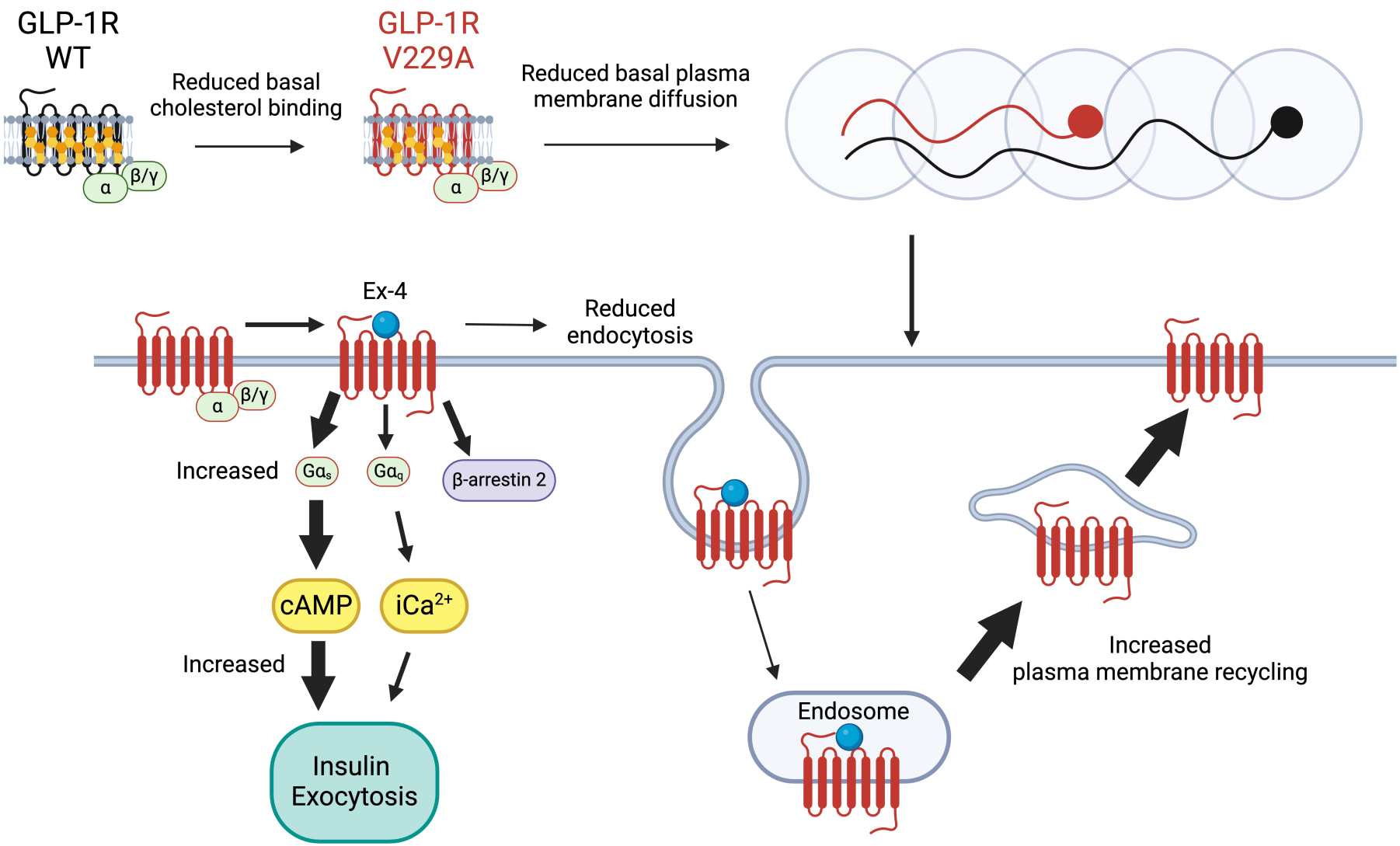
GLP-1R
WT
α
β/γ
Reduced basal
cholesterol binding
GLP-1R
V229A
α
β/γ
Reduced basal plasma
membrane diffusion
Ex-4
α
β/γ
Reduced
endocytosis
Increased
Gαs
Gαq
β-arrestin 2
cAMP
iCa2+
Increased
Insulin
Exocytosis
Endosome
Increased
plasma membrane recycling